On short crested waves: experimental and analytical investigations

Olivier Kimmoun, Hubert Branger, Christian Kharif

On short-crested waves: experimental and analytical investigations

O. Kimmoun [a], H. Branger [b,*], C. Kharif [c]

[a] *Ecole Supérieure d'Ingénieurs de Marseille, IMT Technôpole de Château-Gombert, 13451 Marseille cedex 20, France*
[b] *Institut de Recherche sur les Phénomènes Hors Equilibre, Laboratoire Interaction Océan-Atmosphère, 163 Avenue de Luminy, Case 903, 13288 Marseille cedex 9, France*
[c] *Ecole Supérieure de Mécanique de Marseille, IMT Technôpole de Château-Gombert, 13451 Marseille cedex 20, France*

Abstract – Analytical and experimental investigations were conducted on short-crested wave fields generated by a sea-wall reflection of an incident plane wave. A perturbation method was used to compute analytically the solution of the basic equations up to the sixth order for capillary-gravity waves in finite depth, and up to the ninth order for gravity waves in deep water. For the experiments, we developed a new video-optical tool to measure the full three dimensional wave field $\eta(x,\ y,\ t)$. A good agreement was found between theory and experiments. The spatio-temporal bi-orthogonal decomposition technique was used to exhibit the periodic and progressive properties of the short-crested wave field.

1. Introduction

Most of the studies on the kinematics and dynamics of surface waves were focused for years on two-dimensional wave fields and not many dealt with three-dimensional waves. To have a more realistic description of the sea surface and a better understanding of oceanic phenomena, investigations of three-dimensional wave fields are needed. Due to the complexity of the equations, it is presently not possible to solve the general problem, concerning the interaction of an infinite number of wave trains of an arbitrary frequency distribution, amplitude and wavelength. It thus appeared necessary to restrict the study of these three-dimensional fields to simple patterns: for example, the nonlinear interaction between periodic plane wave trains of constant amplitude could describe rather well the phenomena related to the presence of several swells coming from distant depressions. A simple model is the nonlinear interaction of two similar uniform wave trains coming from two different directions. The generated field is a short-crested wave field. It is a permanent flow, doubly-periodic in two directions of the horizontal plane, and progressive in one of these directions.

Short-crested waves may occur in a number of important maritime situations. Swell being fully reflected off a vertical sea-wall or jetty results in a short-crested wave field being found adjacent to the reflecting wall. Waves propagating down a vertical-walled channel can assume a short-crested wave form when there is a cross-channel variation of the flow pattern. These waves may also occur when a wave train is diffracted behind an obstacle of finite width. These waves are known to have a very steep pyramidal shape that may cause serious damage to vessels or off-shore structures.

The study of this particular type of wave field started at the beginning of the fifties. The first step to solve the Laplace equations, with the two nonlinear boundary conditions was to use a perturbation method. Fuchs [1] obtained a second order solution and Chappelear [2] a third order solution. Both solutions were written in

* Correspondence and reprints; E-mail: branger@pollux.irphe.univ-mrs.fr

dimensional form using an expansion parameter related to the ratio of the waveheight to the wavelength parallel to the wall. This does not allow the standing wave limit to be calculated. Hsu et al. [3] calculated a third order solution in non-dimensional form using an expansion parameter related to the ratio of the waveheight to the wavelength of the incident wave, including the standing wave limit. Roberts [4] made a detailed investigation of the infinite depth case. He computed solutions via a perturbation expansion up to the 27th order in wave steepness and found that the phenomena of harmonic resonance occur at some angles causing the magnitude of some higher coefficients to increase rapidly. The consequence is that the perturbation series has an everywhere zero radius of convergence. Moreover it was possible to obtain convergent solutions nearly up to the maximum wave steepness by using the Padé approximants. Furthermore, Roberts [4] showed that the singularities due to the harmonic resonances are extremely weak and do not in any way affect the coefficients of a finite truncation of the perturbation series. Marchant and Roberts [5] calculated a 35th order solution for waves propagating in water of finite depth. Fenton [6] obtained a third order solution for the short-crested wave problem valid in deep water to calculate the force exerted by the waves on the wall. One of his main findings was the non-intuitive result that the maximum force per unit length was caused by obliquely incident waves rather than standing waves. More recently, Ioualalen [7] determined an analytical solution, up to the fourth order, for the problem of gravity short-crested waves in deep water, using an algebraic manipulator.

Proof of the existence of short-crested waves is a difficult task. However Reeder and Shinbrot [8] investigated the general problem of capillary-gravity short-crested waves in water of finite depth to show that the problem has usually a solution when the ratio of the amplitude to the wavelength is small enough. However, although they can solve 'generally' the problem, they cannot always solve it. There is a set called $\mathcal{M}_d$ (the resonant curves) of the space parameters (the square root Bond number $\sqrt{B_d}$ and the incident wave angle θ) for which the solution is not unique. In particular, it is never possible to get a unique solution for the problem in the absence of surface tension. For this reason Roberts [4] used the Padé approximants, to obtain a solution beyond the singularities. Other methods were developed to compute these three-dimensional wave fields as well. Roberts and Schwartz [9] used the numerical collocation method, for the calculation of symmetric waves in infinite depth. Using the approach developed by Zakharov [10], Badulin et al. [11] calculated analytic solutions of the Hamiltonian problem derived from the exact equations, and highlighted the good agreement which exists between their results and the solutions calculated numerically according to the perturbation method developed by Ioualalen [12]. This 'temporal' Hamiltonian structure is different from the 'spatial' Hamiltonian structure of the wave problem (Benjamin [13] and Zufiria [14]). This latter formulation appears naturally for solutions which are stationary in the reference frame moving with the velocity of the wave. Bridges et al. [15], using the multi-symplectic formulation (a generalization of the temporal and spatial Hamiltonian) developed by Bridges [16], found analytic solutions up to the third order of the problem of three-dimensional capillary-gravity waves in finite depth.

All the studies mentioned previously are related by the forced interaction of two two-dimensional wave trains. Another way to compute three-dimensional patterns is to investigate the bifurcation of Stokes waves. Saffman and Yuen [17] considered the problem of the bifurcation of a uniform, two-dimensional wave train into three-dimensional steady waves of permanent form. They obtained two types of solutions, described as symmetric and skewed wave forms.

The symmetric form is progressive in one direction and standing in the perpendicular direction, like short-crested waves. The skewed form is doubly-periodic in the direction of propagation and in a direction different from the perpendicular direction. Ma [18] used a more general form of the Zakharov equation to calculate the bifurcation of Stokes waves. Meiron et al. [19] used exact equations to calculate symmetric solutions and compare with the weakly nonlinear theory. Martin [20] found symmetric and skewed solutions by solving the nonlinear Schrödinger equations. Finally Bryant [21], on the basis of the full equation, used a Galerkin method

to study the interaction of two periodic wave trains with different wavelengths. This technique, numerically more effective than the collocation method, requires for high steepness, a number of discrete points less than the collocation method. Moreover, its decomposition in Fourier space provides immediate complete information about the spectral modes of the wave solutions. One important point of his study is the idea that the trajectory of the fluid particles is three-dimensional, and that the average direction is different from the propagation direction of the crests.

As was discussed previously, theoretical knowledge of short-crested waves progressed during the last fifty years. On the other hand, to our knowledge, few experimental studies were carried out on the observation of these waves in wave tanks. Su [22] and Su et al. [23], investigated symmetric and skewed three-dimensional forms. The symmetric waves are the result of three-dimensional subharmonic bifurcation of two-dimensional wave trains with steepness higher than 0.25. Other works coming from the study of reflection of oblique swells on offshore constructions or on a jetty, referred to the observation of these specific wave fields. These investigations were often combined with the study of dispersion or diffraction phenomena observed under certain conditions (Perroud [24] and Chen [25] for solitary waves, Nielsen [26], Berger and Kohlhase [27] for Stokes waves). However, in any case, these studies were about the permanent shape of short-crested waves. The papers of Hammack et al. [28,29] referred to the forced interaction of two two-dimensional wave trains, in shallow water. These authors investigated the interaction of two cnoïdal waves, propagating with a small angle to each other. They observed hexagonal patterns, periodic in the direction of propagation and in the perpendicular direction and explained the appearance of the crest oriented in the propagation direction, by the resonant interaction of three waves. The third wave is called the Mach stem (Wiegel [30]) by analogy with shock waves for gases. It was shown that these three-dimensional waves are stable even for high steepness. Nevertheless these experiments did not concern the nonlinear interaction of two two-dimensional Stokes waves propagating at different angles in infinite depth. Using a weakly-nonlinear slowly-varying averaged Lagrangian theory (Whitham [31]) Marchant and Roberts [32] considered the reflection of nonlinear deep-water waves incident onto a wedge of arbitrary angle. They found that the solution is comprised of two regions, within which the wave properties are constant, separated by a wave jump causing the wave field to be modified. Using the same approach Marchant and Roberts [33] extended the work of Peregrine [34] on the circular caustic to include short-crested waves on deep-water due to reflection of the incident wavetrain from such a circular caustic. Our study is mainly motivated by the lack of experimental results on short-crested waves in deep water.

In Section 2 we use a perturbation method to get a sixth order solution for the exact equations of short-crested capillary-gravity waves in water of finite depth. In Section 3, a new imaging wave-slope system is presented and tested, allowing us to measure three-dimensional wave slopes, and then by a recursive integration scheme, the surface topography. In Section 4, the experiments carried out are presented. The results are compared with those given by the analytical model developed in Section 2. Finally, a spatio-temporal technique is used in the last section to characterize the kinematic properties of these waves.

2. Analytical solutions

In order to compare the experimental measurements with the theoretical shape of the short-crested waves, we have calculated analytical solutions of the hydrodynamic equations governing the short-crested wave motion. In this section we present the equations governing the evolution of the short-crested capillary-gravity wave field in water of arbitrary depth, and their solutions.

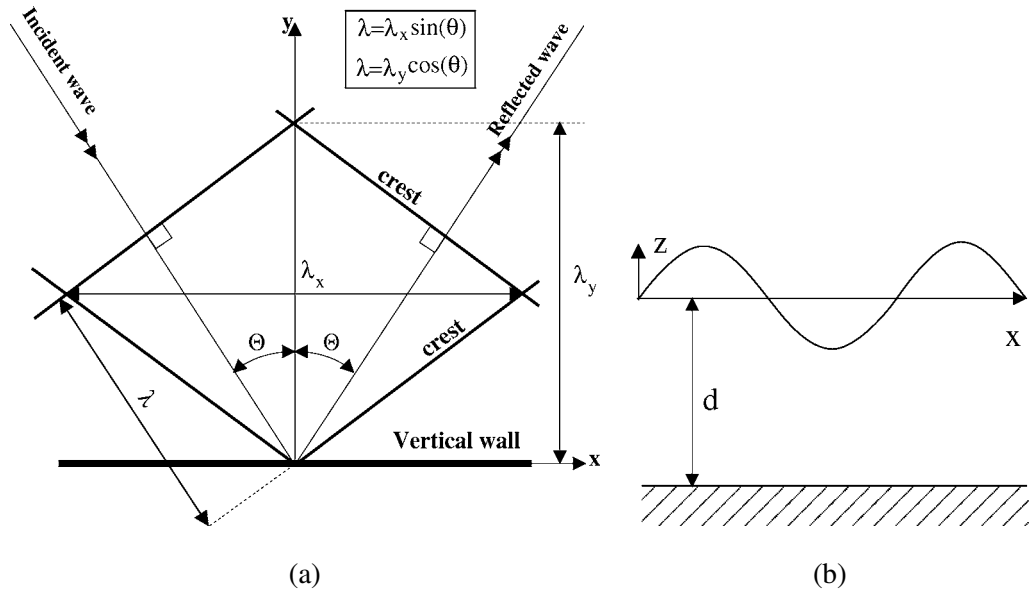

Figure 1. Definition sketch of short-crested waves produced by a sea-wall reflection.

2.1. Hypothesis and equations

The fluid is assumed inviscid, incompressible and the flow irrotational. The short-crested wave field results from the nonlinear interaction of two similar two-dimensional wave train propagating in two different directions (*figure 1*). The governing equations are:

- *Laplace equation*:

$$\nabla^2\phi = 0 \quad \text{for } -d \leqslant z \leqslant \eta(x, y, t). \tag{1}$$

- *Dynamic boundary condition*:

$$\begin{aligned} &g\eta + \phi_t + \frac{1}{2}|\nabla\phi^2| - \frac{T}{\rho}\tau(x, y) = -\frac{p_a}{\rho} + C \quad \text{on } z = \eta(x, y, t) \\ &\text{with } \tau(x, y) = \frac{N(x, y)}{(1 + \eta_x^2 + \eta_y^2)^{3/2}} \\ &\text{and } N(x, y) = \eta_{xx}(1 + \eta_y^2) + \eta_{yy}(1 + \eta_x^2) - 2\eta_{xy}\eta_x\eta_y. \end{aligned} \tag{2}$$

C is a constant introduced to set the mean water level to zero. The subscripts denote partial differentiation.

- *Kinematic boundary condition*:

$$\eta_t + \phi_x\eta_x + \phi_y\eta_y - \phi_z = 0 \quad \text{on } z = \eta(x, y, t). \tag{3}$$

- *Bottom condition*:

$$\phi_z = 0 \quad \text{on } z = -d. \tag{4}$$

- *Wall condition*:

$$\phi_y = 0 \quad \text{on } y = 0, \tag{5}$$

where $\phi(x, y, z, t)$ is the velocity potential, $z = \eta(x, y, t)$ is the equation of the free surface, T is the surface tension, g is the acceleration of gravity, p_a is the atmospheric pressure and ρ is the density. (x, y) are the horizontal coordinates, z is the vertical coordinate and d is the depth.

The wave is assumed to propagate in the x-direction without change of shape. The wavelength of the incident wave is λ. The frequency of the wave is ω. To put all the equations into a non-dimensional form, we set $k = 2\pi/\lambda$ and scale all the variables with respect to the reference length $1/k$ and the reference time $1/\sqrt{gk}$:

$$\begin{cases} \tilde{x} = xk, \quad \tilde{y} = yk, \quad \tilde{z} = zk, \\ \tilde{t} = t\sqrt{gk}. \end{cases}$$

Because of the assumption that the wave is propagating without change of shape we may then find the two functions $\eta(X, Y)$ and $\phi(X, Y, Z)$, 2π periodic in the X and Y directions, the new variables X, Y, Z, being defined by:

$$\begin{cases} X = m\tilde{x} - \omega\tilde{t}, \\ Y = n\tilde{y}, \\ Z = \tilde{z}, \end{cases}$$

with m and n, the non-dimensional x- and y-direction wavenumbers:

$$m = \sin(\theta), \qquad n = \cos(\theta). \tag{6}$$

2.2. Resolution: perturbation method

η, ϕ, ω and C are expanded as power series in the small arbitrary parameter ϵ:

$$\begin{cases} \phi(X, Y, Z) = \sum_{R=1}^{\infty} \phi_R(X, Y, Z)\epsilon^R, \\ \eta(X, Y) = \sum_{R=1}^{\infty} \eta_R(X, Y)\epsilon^R, \\ \omega = \sum_{R=1}^{\infty} \omega_R\epsilon^R, \\ C = \sum_{R=1}^{\infty} C_R\epsilon^R. \end{cases} \tag{7}$$

The dimensionless velocity potential at the free surface may be expressed in terms of the Taylor expansion at $Z = 0$ instead of $Z{=}\eta$:

$$\begin{aligned} \phi(X, Y, Z = \eta) = {} & \sum_{R=1}^{7} \phi_R(X, Y, 0)\epsilon^R + \sum_{R=1}^{7} \eta_R\epsilon^R \sum_{R=1}^{7} \frac{\partial \phi_R}{\partial z}\epsilon^R \Big|_{z=0} \\ & + \cdots + \left[\sum_{R=1}^{7} \eta_R\epsilon^R\right]^7 \sum_{R=1}^{7} \frac{\partial^7 \phi_R}{\partial z^7}\epsilon^R \Big|_{z=0} + \mathrm{O}(\epsilon^8). \end{aligned} \tag{8}$$

The potential $\phi(X,Y,Z)$ can be written as

$$\phi(X,Y,Z=\eta)=\sum_{R=1}^{7}a_R(X,Y)\epsilon^R+\mathrm{O}(\epsilon^8), \tag{9}$$

$$\text{with } a_R(X,Y)=\phi_R(X,Y,0)+\phi_R^+(X,Y,0). \tag{10}$$

The curvature τ(X,Y) may be developed in terms of a series expansion:

$$\tau(X,Y)=N(x,y).\left(1-\frac{3}{2}\left(m^2\eta_x^2+n^2\eta_y^2\right)+\frac{15}{8}\left(m^2\eta_x^2+n^2\eta_y^2\right)^2\right), \tag{11}$$

and can be written as

$$\tau(X,Y)=\sum_{R=1}^{7}\tau_R\epsilon^R+\mathrm{O}(\epsilon^8), \tag{12}$$

$$\text{with } \tau_R=m^2\eta_{R,XX}+n^2\eta_{R,YY}+\tau_R^+. \tag{13}$$

$\phi_R^+(X,Y,0)$ and τ_R^+ are developed in Appendix A up to the fourth order. The higher order terms are too long to be given here. $\eta_{R,XX}$ and $\eta_{R,YY}$ are the second derivatives of η_R with respect to X and Y respectively. The steepness of the wave field is defined as:

$$h=\frac{1}{2}\left(\eta(0,0)-\eta(\pi,0)\right), \tag{14}$$

which is the half non-dimensional peak-to-trough height since the peak of the wave will be fixed at $(X,Y)=(0,0)$. After substitution into the equations and grouping like powers of ϵ, we get an infinite system of equations. The equations (1)–(3) yield:

- *Laplace equation*

$$m^2\phi_{R,XX}+n^2\phi_{R,YY}+\phi_{R,ZZ}=0 \quad \text{for } -d\leqslant z\leqslant\eta(X,Y). \tag{15}$$

- *Kinematic boundary condition*

$$\omega_0\eta_{R,X}+\phi_{R,Z}=A_R \quad \text{on } Z=0, \tag{16}$$

$$\text{with } A_R=-\phi_{R,Z}^+ +\sum_{s=1}^{R-1}-\omega_{R-s}\eta_{s,X}+m^2a_{R-s,X}\,\eta_{s,X}+n^2a_{R-s,Y}\,\eta_{s,Y}. \tag{17}$$

- *Dynamic boundary condition*

$$\eta_R-\omega_0\phi_{R,X}-\kappa\left(m^2\eta_{R,XX}+n^2\eta_{R,YY}\right)=B_R+C_R \quad \text{on } Z=0, \tag{18}$$

$$\begin{aligned}\text{with } B_R=&\,\omega_0\phi_{R,X}^+ +\kappa\tau_R^+\\ &+\sum_{s=1}^{R-1}\left(\omega_s a_{R-s,X}+m^2a_{s,X}a_{R-s,X}+n^2a_{s,Y}a_{R-s,Y}+a_{s,Z}a_{R-s,Z}\right).\end{aligned} \tag{19}$$

κ is the dimensionless capillary number defined by $\kappa=\frac{Tk^2}{\rho g}$. This parameter represents the reverse of the Bond number B_d, and measures the ratio between capillarity and gravity effects.

2.3. Solutions

We will merely outline the solutions and refer the reader to the work of Kimmoun [35] for all the details.

The first order solution can be written as

$$\begin{cases} \phi_1 &= \omega_0 \dfrac{\cosh(Z+d)}{\sinh(d)} \sin(X)\cos(Y), \\ \eta_1 &= \cos(X)\cos(Y), \\ \omega_0^2 &= (1+\kappa)\tanh(d), \\ C_1 &= 0. \end{cases} \tag{20}$$

The form of this first order solution restricts the Rth order solution having the form:

$$\eta_R = \sum_{p,q}^{R} a_{Rpq} \cos(pX)\cos(qY), \tag{21}$$

$$\phi_R = \sum_{p,q}^{R} b_{Rpq} \sin(pX)\cos(qY)\cosh\left(\alpha_{pq}(Z+d)\right), \quad \text{where } \alpha_{pq}^2 = m^2p^2 + n^2q^2. \tag{22}$$

The right-hand side of the kinematic and dynamic boundary conditions are trigonometric products resulting from previous orders, so it may be expressed in the form:

$$\begin{cases} A_R = \displaystyle\sum_{p,q}^{R} Ad_{Rpq} \sin(pX)\cos(qY), \\ B_R + C_R = \displaystyle\sum_{p,q}^{R} Bd_{Rpq} \cos(pX)\cos(qY). \end{cases} \tag{23}$$

For (p,q) given, equations (16) and (18) yield

$$\begin{cases} -\omega_0\, p a_{Rpq} + \alpha_{p,q} \sinh(\alpha_{pq}d) b_{Rpq} = Ad_{Rpq}, \\ (1+\kappa\alpha_{pq}^2)\, a_{Rpq} - \omega_0\, p \cosh(\alpha_{pq}d) b_{Rpq} = Bd_{Rpq}. \end{cases} \tag{24}$$

So the solutions are

$$\begin{cases} a_{Rpq} = \dfrac{\alpha_{pq} \tanh(\alpha_{pq}d)\, Bd_{Rpq} + \omega_0\, p\, Ad_{Rpq}}{(1+\kappa\,\alpha_{pq}^2)\,\alpha_{pq} \tanh(\alpha_{pq}d) - \omega_0^2\, p^2}, \\ b_{Rpq} = \dfrac{(1+\kappa\,\alpha_{pq}^2)\, Ad_{Rpq} + \omega_0\, p\, Bd_{Rpq}}{(1+\kappa\,\alpha_{pq}^2)\,\alpha_{pq} \sinh(\alpha_{pq}d) - \omega_0^2\, p^2 \cosh(\alpha_{pq}d)}. \end{cases} \tag{25}$$

The short-crested wave steepness h, which is an input of the analytical model, is a polynomial function of the small expansion parameter ϵ: $h = P(\epsilon)$. The perturbation parameter ϵ can be easily found by inverting the polynomial series: $\epsilon = P^{-1}(h)$.

The analytical solutions were calculated up to the 'sixth order' using XMAPLE and extend previous works about short-crested waves to higher order. For pure gravity short-crested waves in water of finite depth and for

capillary-gravity short-crested waves in deep water, the solutions were calculated up to the 'seventh order'. For pure gravity short-crested waves in deep water, this method allows us to calculate a solution up to the 'ninth order'. The second order solution and the frequency at the third order are given in the Appendix B. The sixth order solution is a sum of thousands of different terms.

Figures 2 and *3* show the shape of typical analytical results of the short-crested wave field problem. The picture *figure 2(a)*, corresponds to short wavelength and small depth. In this case, patterns exhibit hexagonal shapes. The picture *figure 2(b)* is specific to waves in water of finite depth with steep crests and flat troughs. The picture *figure 3(a)* is characteristic of capillary waves with round crests and the picture *figure 3(b)* is specific to steep short-crested gravity waves with the pyramidal shape described by Roberts [4].

3. Experimental technique

3.1. Introduction

The precise measurement of the spatial and time characteristics of a wave field is still an open problem, even in a laboratory environment. Only optical methods allow the determination of the water surface topography without disturbing the waves. Well known techniques are the 'stereo-photography' (Shemdin et al. [36]), the 'scanning laser slope gauge' (Bock and Hara [37]) and the 'shape from shading' (Jähne and Riemer [38]) methods. 'Stereo-photography' was mainly used in open field environment (Banner et al. [39]), but careful analysis showed that the height resolution was achieved only for waves with wavelengths larger than 100 times the camera horizontal resolution (Jähne and Schultz [40] and Branger et al. [41]). The 'laser slope gauge' gives precise results in the wavenumber and frequency domains. However, this device is not dedicated to give instantaneous surface topography (Bock and Hara [37]). The 'shape from shading' technique was first developed by Keller and Gotwols [42] and Jähne and Waas [43]. This method, based on the lights refraction at the water surface, gives one component of the slopes of the waves over a rectangular area. Jähne and Riemer [38] have improved the technique by measuring the two components of the slopes. Unfortunately these two components were not measured simultaneously and the surface topography determination was not possible (Keller et al. [44]). Recently Zhang and Cox [45] made a major improvement using a color screen with suitable 2-D color patterns. This apparatus was able to detect simultaneously the slope amplitude and direction. The ultimate resolution was sufficient to study the waveform of capillary waves generated in a wind-wave tank (Zhang [46]). The area of the water surface examined was about 20×20 cm^2.

Our application needed a larger area, typically 60×60 cm^2. A new imaging wave-slope system based on a combination of the Jähne and Riemer [38] and Zhang and Cox [45] techniques, with a two-colored submarine lighting box, a color camera and a RGB laser video-disk recorder was developed. Moreover, we developed a de-noising integration procedure to obtain the 3-D water surface elevation over the full area. The time history of the water surface was scanned by successive photographs taken at a rate of 25 frames per second.

3.2. Optical setup

The 'shape from shading method' is based on light propagation through a diffusive medium and light refraction by the water surface. The water slope measurements by light refraction has been described in details by Jähne and Riemer [38]. The source of the light is entirely from below the water surface. A lighting box located on the floor of the tank contains an aqueous suspension of unisphere latex polystyrene particles. The box is illuminated on one side by a row of bright lamps. The aqueous solution acts as a diffusive medium and induces an exponential decay of the light. Images of the illuminated surface are acquired with a camera located

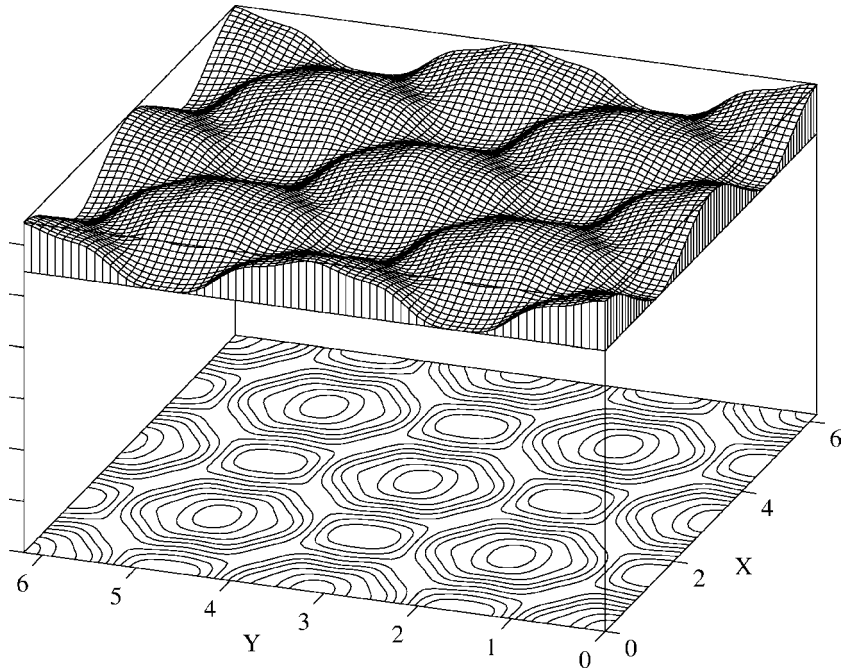

(a)

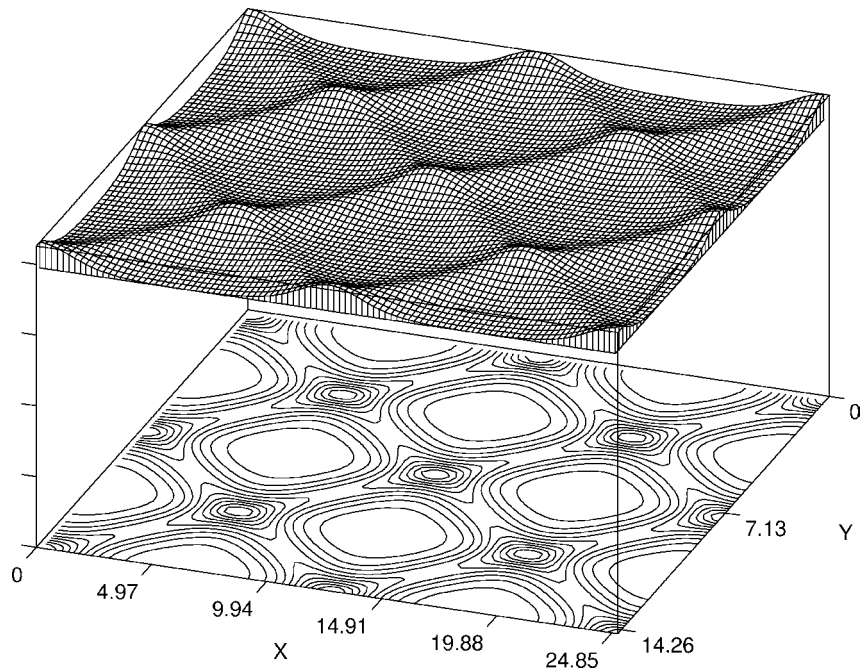

(b)

Figure 2. Representation of the analytical surface shape for (a) capillary-gravity short-crested waves in water of finite depth: $h = 0.25,\ \theta = 30^\circ,\ \kappa = 2.92$ ($\lambda = 1$ cm), $d/2\pi = 0.2$, (b) pure gravity short-crested waves in water of finite depth, $h = 0.25,\ \theta = 30^\circ,\ d/2\pi = 0.1$.

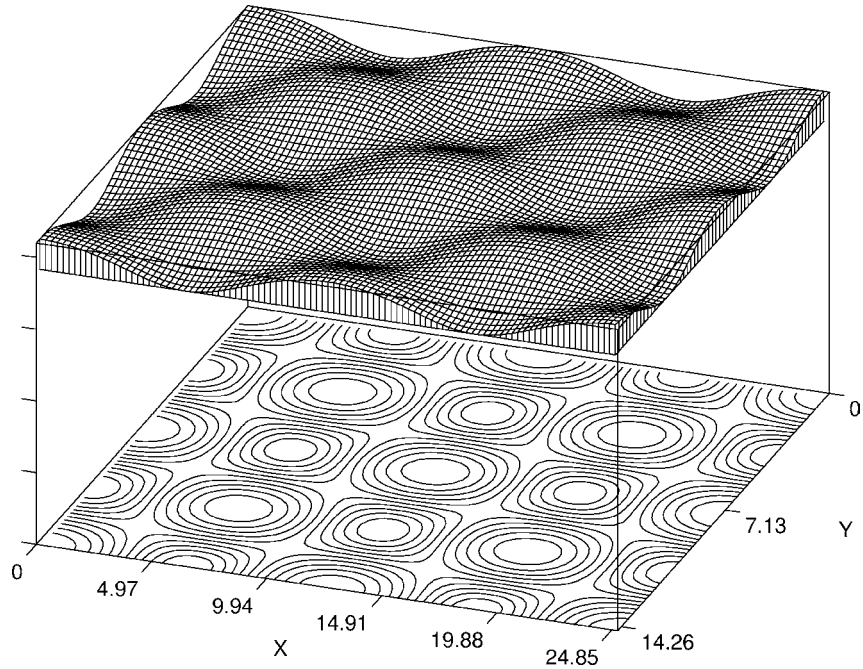

(a)

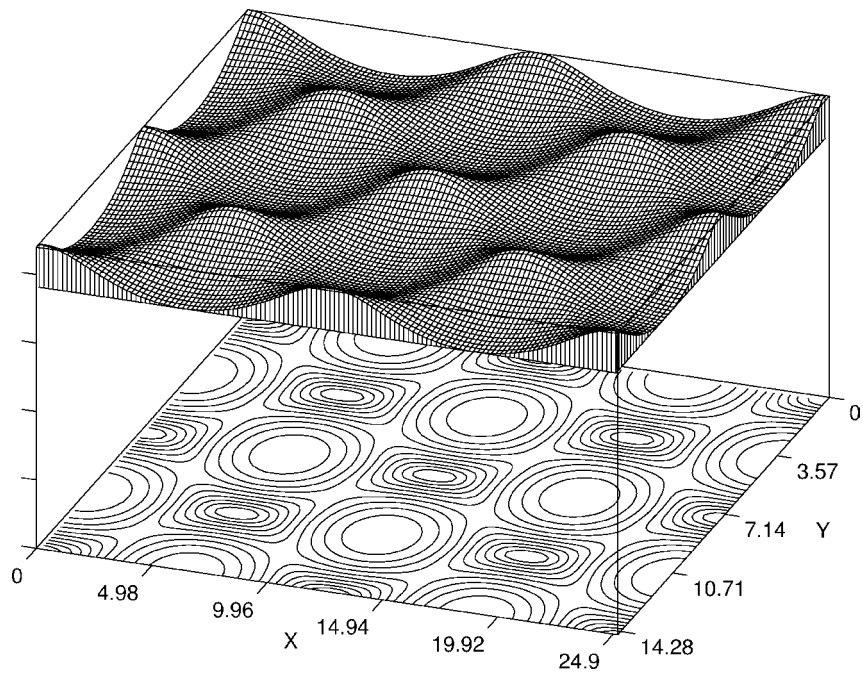

(b)

Figure 3. Representation of the analytical surface shape for (a) capillary-gravity short-crested waves in deep water: $h = 0.30,\ \theta = 30^{\circ},\ \kappa = 2.92$ ($\lambda = 1$ cm), (b) pure gravity short-crested waves in deep water, $h = 0.3,\ \theta = 30^{\circ}$.

on the top of the facility and looking vertically downward. When waves propagate, light rays coming from the underwater screen box are deflected by the slope of the wavy surface. The gradient of light intensity is then modulated by the waves. If the water-depth is large compared with the wave amplitude, then the component of the wave slope in the direction of lighting, s, can be found, to first order approximation, with a simple geometric law function of the brightness of the wavy surface image I and the brightness of the surface at rest I_0 (Jähne and Riemer [38]):

$$s = \frac{1}{\alpha} \frac{I - I_0}{I_0}, \tag{26}$$

where α depends on the water depth and the light intensity gradient of the diffusor box. If two floodlights are used with two different monochromatic wavelengths in two different directions, then two components of the wave-slope can be measured simultaneously. The water elevation is calculated by integrating the two-slope components.

For our experiments, we used narrow-banded red and green lights which induced exponential decay of red intensity in the x direction and green intensity in the y direction. A schematic view of the lighting box is displayed in *figure 4*. The dimensions of the box were $120 \times 120 \times 20$ cm^3. The box was illuminated by two ramps of ten 100 W halogen lamps located beside each lateral screen wall. A diffusor medium was put in front of the lamps to obtain an homogeneous lighting. The light intensity of each ramp was controlled by a voltage variator. The screen on the x-side was covered with a monochromatic gelatin green filter (Kodak Wratten Filter reference 29). The screen on the y-side was covered with a monochromatic gelatin red filter (Kodak Wratten Filter reference 58). We used these two narrow-band filters because their central color wavelengths were far from each other and only 0.6% of the transmitted light energy overlaps (*figure 5*). The latex particles diffused the light and induced an exponential decay of the red and green intensities.

A side view of the video experimental setup is shown in *figure 6*. The image acquisition apparatus consists in (a) a three 'charge coupled device' color video camera, (b) a laser video-disk recorder, and (c) a Unix workstation with a video acquisition card.

(a) The Sony DXC-930P color video camera produces high quality colored pictures thanks to the use of a high performance three-chip Charge Coupled Device (CCD) having 752×582 effective picture elements that allows *separated acquisitions* of the red, green and blue component of the light. The peaks of the CCD received red and green light spectra were close to the peaks of the transmitted red and green filtered light spectra. The total overlapping of the two colors was less than 4% (*figure 5*). The camera has a high sensitivity and a high signal-to-noise ratio (56 dB). The shutter speed can be set manually to avoid fuzzy images of moving waves. A Sony VCL-712 zoom lens with a varying focal length was mounted on the camera, so it was possible to adjust the size of the observational field of view without moving the camera. The spatial resolution depended on the focal length. Typically, the picture size was 110×75 cm^2, which gives an horizontal resolution of 0.15×0.15 cm^2 per pixel.

(b) The Sony 4000-P laser video-disk recorder (LVR) was connected to the camera through 4 cables (red, green, blue and synchronization connections). The laser video-disc has a capacity of 76500 images with a maximal recording rate of 25 video frames per second. The LVR is a very convenient system: each image is referenced by a number and can be viewed directly, as long as required, without being altered.

(c) For digitization and numerical processing, the LVR was connected to an Indy Silicon Graphics Workstation through an S-VHS video acquisition card. Color information (chrominance) and light intensity (luminance) were acquired separately, which was of interest for our use. However, an RGB video card would have been better to acquire separately the red and green components of the light. Unfortunately such a card was not available on the workstation during the experiments.

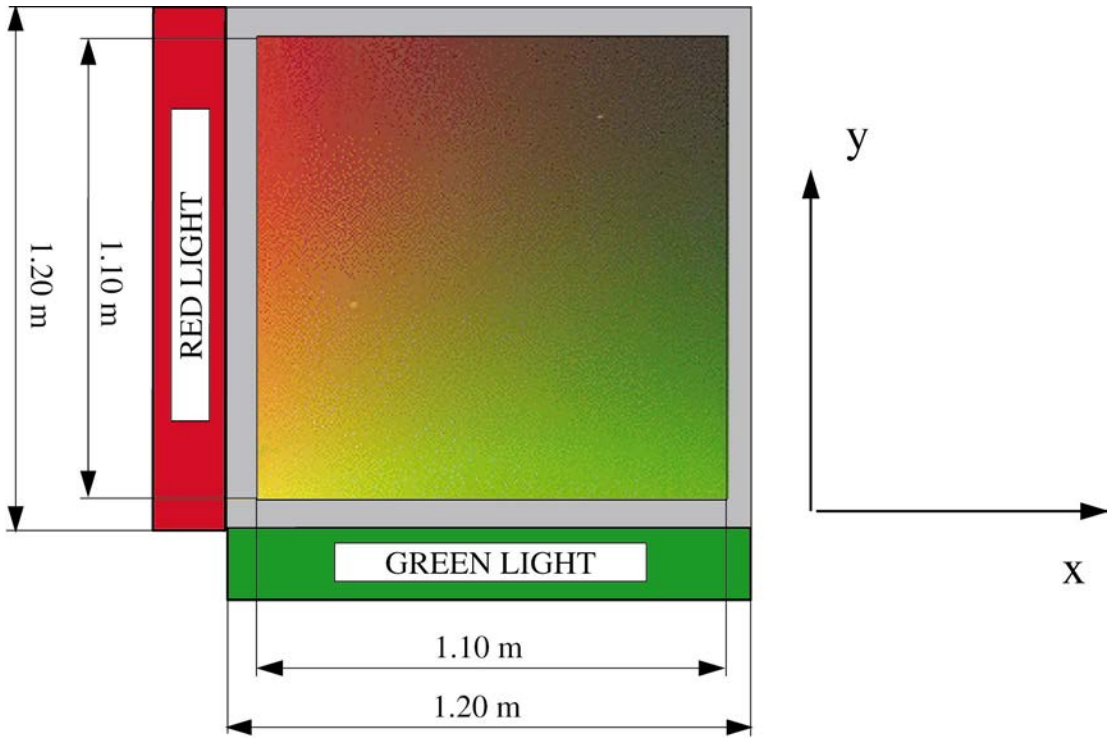

Figure 4. The light box seen from above, the water surface being at rest.

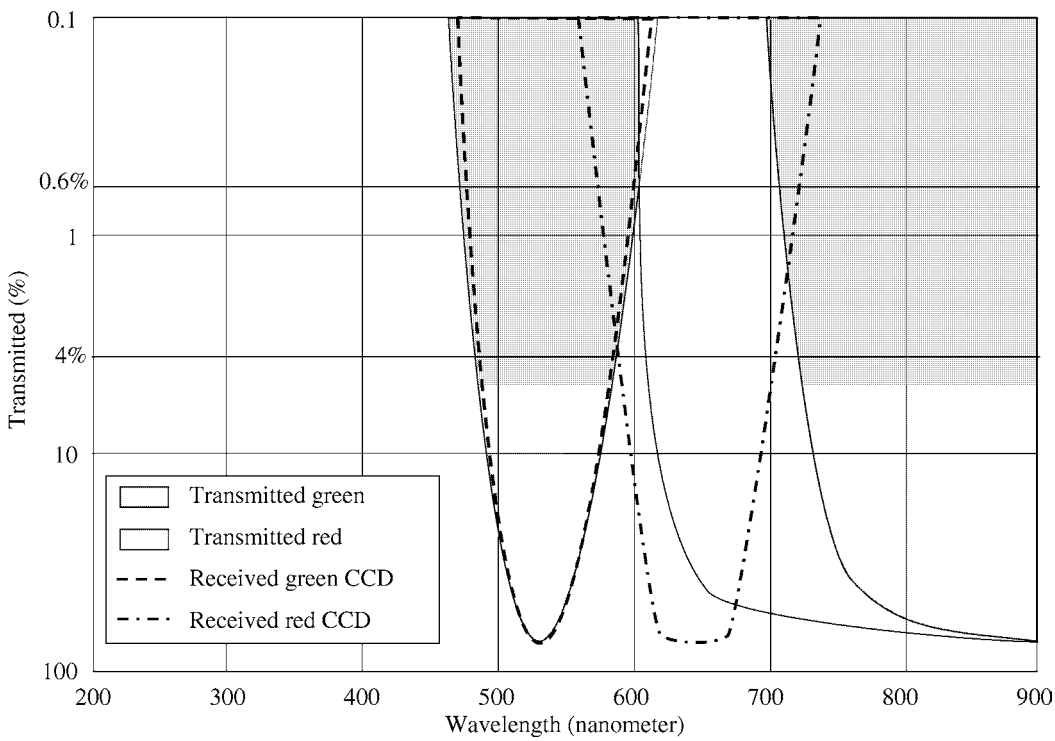

Figure 5. Kodak filter transmitted spectra and camera CCD received spectra.

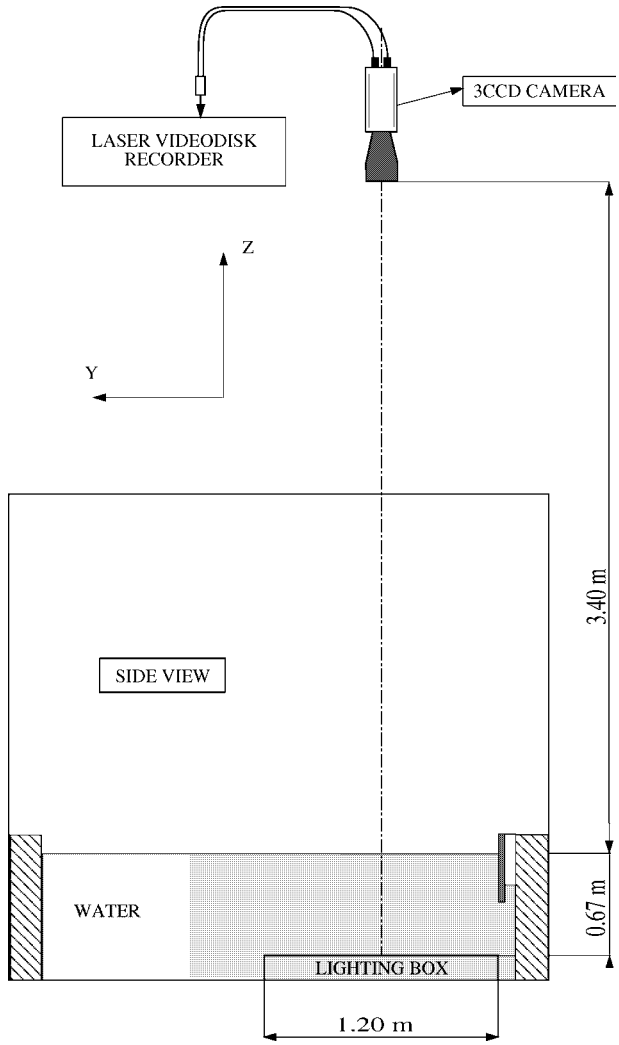

Figure 6. Side view of the video experimental apparatus.

3.3. Slope measurements

The distance between the water surface and the camera was 340 cm and the water depth above the underwater light box was 67 cm. These values are high compared with the maximum wave-height of the short-crested waves, (i.e. 2 cm). So the first order approximation of Eq. (26) can be used (Jähne and Riemer [38]). The two-components of the wave-slope s_x and s_y are determined by:

$$\begin{cases} s_x = \dfrac{1}{\alpha_{\text{red}}} \dfrac{I_{\text{red}} - I_{0\,\text{red}}}{I_{0\,\text{red}}}, \\ s_y = \dfrac{1}{\alpha_{\text{green}}} \dfrac{I_{\text{green}} - I_{0\,\text{green}}}{I_{0\,\text{green}}}. \end{cases} \tag{27}$$

- $I_{0\,\text{red}}$ and $I_{0\,\text{green}}$ are the red and green components of the brightness of the surface at rest.

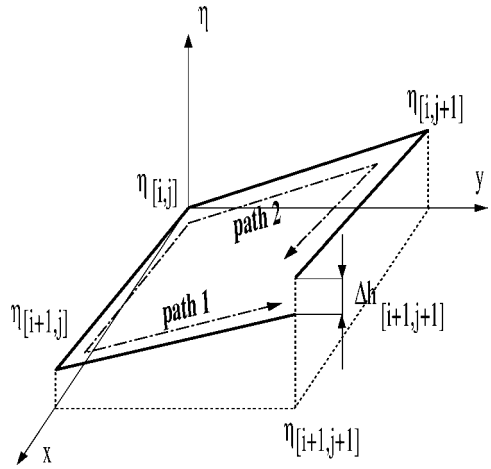

Figure 7. Integration scheme.

- I_{red} and I_{green} are the red and green components of the brightness of the wavy surface.
- α_{red} and α_{green} depend on the red and green light intensity gradients and on the water depth at rest.

To reduce the background noise due to image digitization, we applied an adaptative two dimensional Wiener filter based on statistical estimations from the local neighborhood of 5×5 pixels^2 (ref. Matlab Image Processing Toolbox). This filter acts as a low passband filter with a cutoff wavelength of 7.5 mm. Near the red source there was a saturation of the light intensity, and far from the red and green sources, the camera was not sensitive enough to measure a significant decay of light. The domain where the red and green light decayed exponentially, within a relative error of 1%, was finally limited to a square area of 45×45 cm^2 (Kimmoun [35]).

3.4. Water elevation

The elevation wave field $\eta(x, y)$ over the sample area may be obtained by integrating the measured x and y wave slopes $\eta_x(x, y)$ and $\eta_y(x, y)$. However, the residual noise of the measurements and the approximations used to compute the slopes from the image lead to the 'non integrability' of the slopes wave field, i.e.:

$$\int_x \eta_x(x, y)\,\mathrm{d}x \neq \int_y \eta_y(x, y)\,\mathrm{d}y. \tag{28}$$

As shown in *figure 7*, the water elevation at pixel $(i+1, j+1)$ can be computed from water elevation at pixel (i, j) using two different paths :

$$\begin{cases} \eta_{i+1,j+1}(\text{path}_1) = \eta_{i,j} + \dfrac{\Delta x}{2}\big(\eta_x(i+1, j) + \eta_x(i, j)\big) + \dfrac{\Delta y}{2}\big(\eta_y(i+1, j+1) + \eta_y(i+1, j)\big), \\ \eta_{i+1,j+1}(\text{path}_2) = \eta_{i,j} + \dfrac{\Delta x}{2}\big(\eta_x(i, j+1) + \eta_x(i+1, j+1)\big) + \dfrac{\Delta y}{2}\big(\eta_y(i, j) + \eta_y(i, j+1)\big). \end{cases} \tag{29}$$

The shift due to non integrability of the surface,

$$\Delta h_{i+1,j+1} = \eta_{i+1,j+1}(\text{path}_1) - \eta_{i+1,j+1}(\text{path}_2) \tag{30}$$

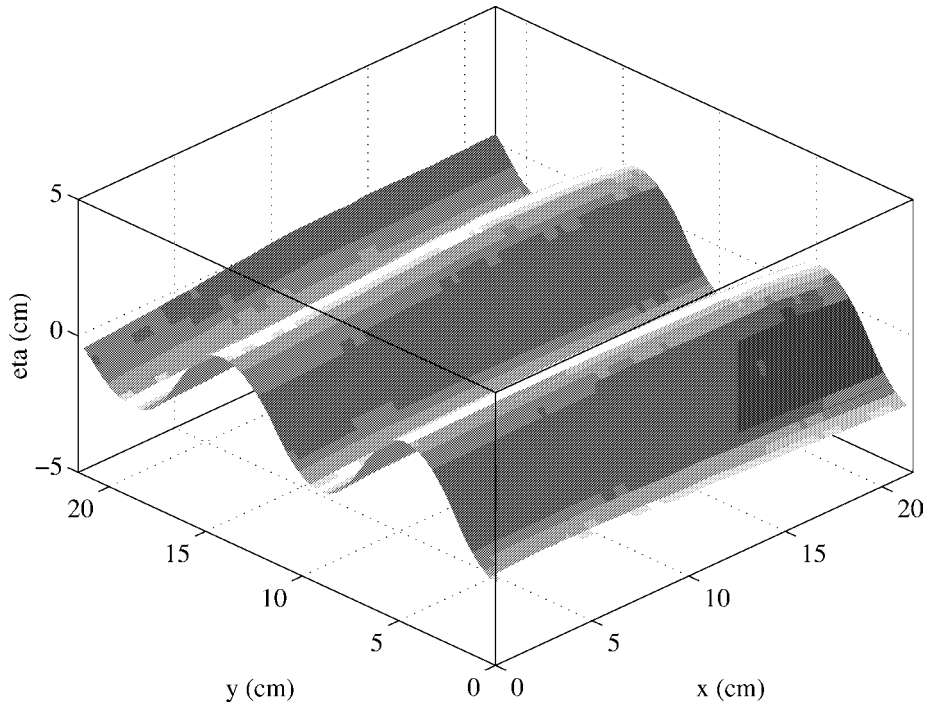

Figure 8. Measured elevation of the frozen plastic wave, oriented at 0°.

can be minimized by a factor γ, by correcting the x and y slopes at each pixel:

$$\begin{cases} \eta_{x,\text{corrected}}(i,j) = \eta_x(i,j) - \dfrac{1}{\gamma}\dfrac{\Delta h}{\Delta x}, \\ \eta_{y,\text{corrected}}(i,j) = \eta_y(i,j) + \dfrac{1}{\gamma}\dfrac{\Delta h}{\Delta y}. \end{cases} \tag{31}$$

By applying recursively this correction to every path over all the domain, the shift Δh may be minimized up to a threshold value, thus giving a valuable water elevation wave field.

3.5. Assessment of the optical device

Jähne and Riemer [38] and Keller et al. [44] used a 'frozen wave' to calibrate their water slope measurements. We used a similar technique to prove the availability of our new optical device to measure the water surface topography. The precision of the optical setup was evaluated with a frozen wave built from a thin transparent foil bent into the shape of a plane sinusoïdal wave by a surrounding frame. The rigid wave was put onto the water in such a way that the space below the foil was filled with water. The sinusoidal frozen wave had a wavelength of $\lambda = 10$ cm with an peak-to-trough wave height of 3.7 cm. Due to the high slopes of the wave (the maximum slope was 66°), optical rays coming from the edge of the lighting box were deflected outside the camera. So the measurement area was reduced to 22×22 cm^2. A 3D plot of the elevation using the new integration method is shown in *figure 8*. This representation shows qualitatively the ability of the method to reconstruct the water elevation wave field. The crest-to-trough and wavelength measured by the optical device are compared with the actual values in *table I*, for two plastic wave directions. The errors, less than 4% for

Table I. Measured amplitude ($2a_{\text{exp}}$) and wavelength (λ_{exp}) for two directions of the calibration wave; absolute and relative comparisons with the actual values.

θ	$2a_{\text{exp}}$	λ_{exp}	e_{2a}	$e_{2a}\%$	e_λ	$e_\lambda\%$
0°	3.65 cm	9.60 cm	0.05 cm	1.35%	0.4 cm	4%
90°	3.57 cm	9.70 cm	0.13 cm	3.4%	0.3 cm	3%

Table II. Angle (θ_{exp}) and wavelength (λ_{exp}) of the plastic wave computed from spectral analysis of the measured data: comparisons with the actual values θ_{actual} and λ_{actual}.

θ_{actual}	θ_{exp}	e_θ	λ_{actual}	λ_{exp}	e_λ	$e_\lambda\%$
0°	0°	0°	10.0 cm	10.1 cm	0.1 cm	1%
25°	26°6	1°6	10.0 cm	9.90 cm	0.1 cm	1%

elevation and wavelength, give an idea of the relatively good estimation provided by the system, even for a high steepness geometry. Measured wavelength and direction, calculated by two-dimensional spectral analysis, for two other plastic wave configurations, are presented in *table II*. The results give errors less than 2° for the direction and 1% for the wavelength.

In conclusion, we assess that this new two-colors shape for shading technique, combined with a new recursive integration scheme, provides surface topography over the selected area within a precision of 4% for the elevation, 1% for the wavelength and 2° for the direction.

4. Experiments

4.1. Experimental setup

The aim of the experiments was to measure three-dimensional properties in time and space of a short-crested wave-field and to compare the results with the analytical development described in Section 2.

The experiments were conducted in the large IRPHE wind-wave tank. The facility (40 m long, 3 m wide and 3 m high) is described in details by Coantic et al. [47]. For experimental convenience, the short-crested wave-field was generated by the reflection of an incident wave train on a vertical wall. A schematic view of the experimental setup is shown in *figure 9*. An electro-mechanical plunging wave-maker was installed on a traveling support. The amplitude a, frequency ω, and direction of the initial wave-train θ, were adjustable. Transverse propagation of incident waves was limited by two side-walls (wharfs 1 and 3 in *figure 9*). Incident waves were reflected along wharf 2. Interaction of incident and reflected plane waves produced the required short-crested wave patterns which were measured with the imaging device described in Section 3. Wave absorbers were put on the opposite sidewall to avoid backward wave reflection. A capacitance wire wave gauge was located halfway between the wave-maker and the location of the lighting box. Elevation of the incident waves were measured with a precision of 0.3 mm. The water surface was cleaned before each experiment by blowing a light wind so that any surface film was collected on a filter at the end of the tank. For each run, a time series of water elevation was acquired at a frequency of 100 Hz during two minutes. Spectral analysis gave the dominant wave frequency, $\omega = 2\pi\ f$. The wavelength, $\lambda = 2\pi/k$, was computed through the standard dispersion relationship:

$$\omega^2 = g\,k\left(1 + (ak)^2\right) + \frac{T}{\rho}k^3 \tag{32}$$

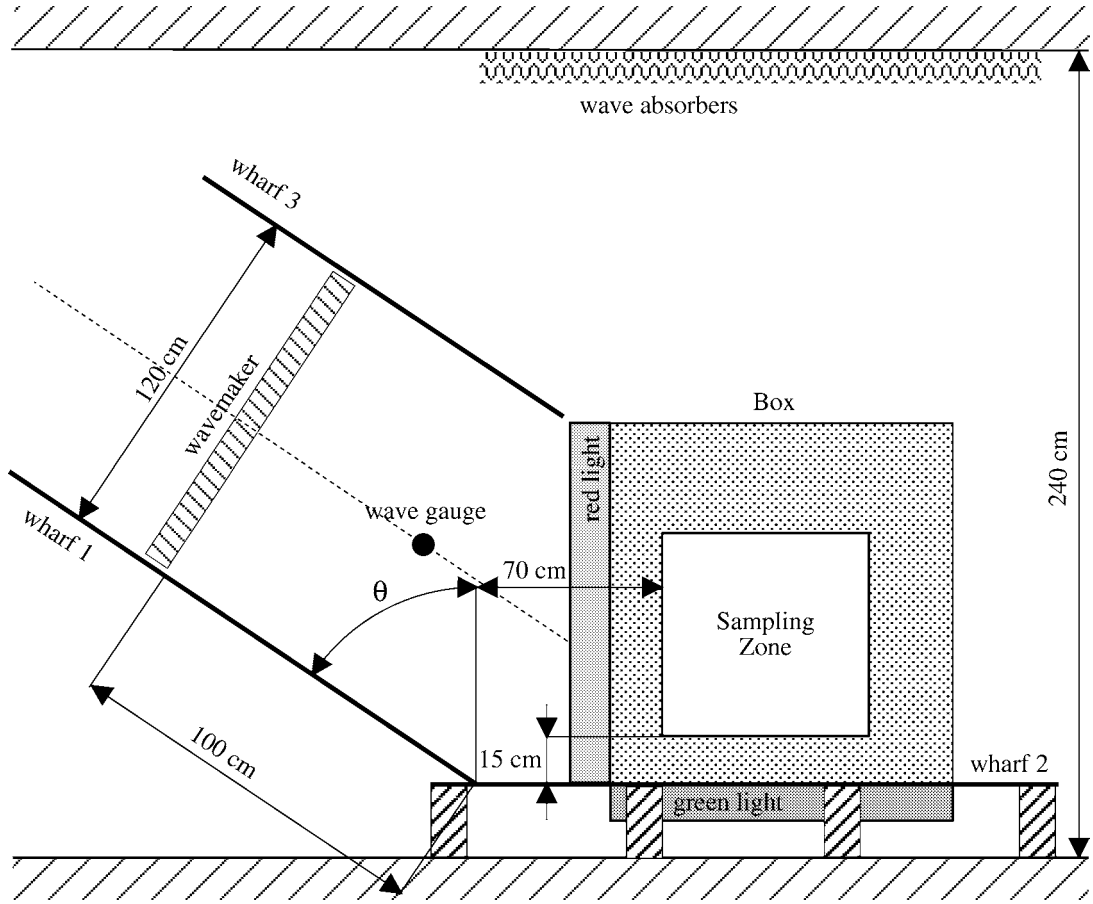

Figure 9. Schematic top view of the experimental setup.

which gives:

$$k = A^{1/3} - \frac{g}{3\left(ga^2 + \frac{T}{\rho}\right)A^{1/3}} \tag{33}$$

with

$$A = \frac{\omega^2}{2\left(ga^2 + \frac{T}{\rho}\right)} + \frac{1}{18}\frac{\sqrt{4g^3 + 27\omega^4\left(ga^2 + \frac{T}{\rho}\right)}\sqrt{3}}{\left(ga^2 + \frac{T}{\rho}\right)^{3/2}}. \tag{34}$$

4.2. Experimental conditions

A first series of experiments was conducted to determine the experimental conditions for which it was possible to generate a steadily propagating short-crested wave field in the facility. *Figure 11* is a camera view of a high steepness generated short-crested wave field showing qualitatively the characteristic pyramidal form of the crests. The range of the input parameters (amplitude, frequency and incidence angle of the wave-maker) was limited by experimental constraints. Firstly the range of available amplitude and frequency values was reduced,

Table III. Experimental conditions: incident wave characteristics.

Experiment number	Incidence angle	Incident f (Hz)	Incident $2a$ (cm)	Incident λ (cm)	Incident ak
1		3.71	1.10	12.45	0.28
2	45°	4.30	0.75	9.35	0.25
3		4.45	0.49	8.48	0.18
4		3.66	0.66	12.18	0.17
5	35°	4.05	0.54	10.06	0.17
6		4.64	0.44	7.83	0.18

due to electro-mechanical constraints and to the fixed triangular profile of the wave-maker section. Secondly the generation of steep Stokes waves (incident wave steepness larger than 0.25) produces perturbations due to three-dimensional instability (see Mc Lean et al. [48] and Mc Lean [49] for numerical investigations; Su [22] and Su et al. [23] for experiments) and Benjamin–Feir type instability (Benjamin and Feir [50]). However in our experimental configuration, Benjamin–Feir instabilities did not appeared because the measurements area was always located at less than twenty-four dominant wavelengths away from the wave-maker (Lake and Yuen [51] and Melville [52] have shown that, for the same conditions, these modulations need more than fifty wavelengths to appear).

An other phenomenon arises when the incidence angle θ, is relatively large (i.e. greater than 60°). The singularity, due to the intersection between wharf 1 and wharf 2, causes the apparition of the 'Mach stem'. An example of the Mach reflection observed in the tank for an incidence angle of 60° is shown in *figure 10*. The Mach stem phenomenon was described for the case of periodic water waves by Nielsen [26] and Berger and Kohlhase [27]: when the incidence angle is large, a third wave (called the stem) is generated which intersects the wall normally. The incident crest, the reflected crest, and the stem crest meet at a point some distance away from the wall. The wave amplitude along the barrier, that is, the stem height, increases down-wave for a finite distance and then levels off gradually. At any station this amplitude increases with the angle of incidence. The width of the stem region, which generally increases with distance along the wall, is larger with larger incidence angle and shorter incident wavelength.

Finally, for the present study, we selected six experimental conditions for which the Mach effect described above was not observed. The incident wave characteristics measured by the wave gauge for each run are summarized in *table III*. The incident wavelength λ was computed from the measured frequency f using relations (32)–(34). All these experimental conditions are those of deep water ($d/\lambda > 5$). Stable experimental conditions were obtained for experiments n° 2 to 6, but slight instabilities were observed during experiment n° 1 which corresponds to the highest incident wave steepness ($ak = 0.28$).

4.3. Results and comparisons

For the six experiments performed, the slopes were calculated in the two horizontal directions and the topography of the water surface was computed with the method described in Section 3.4. The acquisition duration for every experiment was about twenty seconds at a rate of twenty-five images per second. From these thousands of images, hundreds of pictures were digitalized and numerically treated. For simplicity, we first discuss in detail results from experiment n° 6. This case is typical of waves in the range of short-gravity waves ($B_d = \rho g / Tk^2 = 20.18$). Results from the other experiments will be presented later.

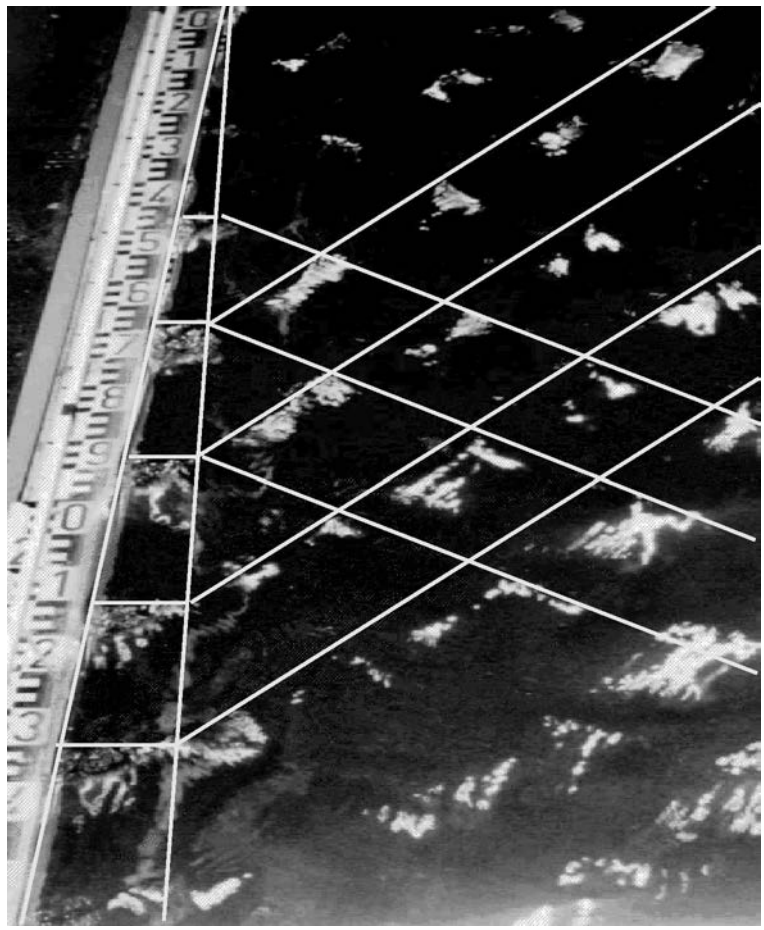

Figure 10. Overhead image showing Mach reflection. Incident waves ($\theta = 60°$) are coming from the top right of the picture; wharf 2 is on the left. The white lines show the location of the wave fronts.

4.4. Experiment n° 6

Figure 12 gives an example of the short-crested wave slopes, $\eta_x(x, y)$ and $\eta_y(x, y)$, measured by the optical device. Pyramidal waves appear to be very steep: wave slope values extend from -0.6 to $+0.6$. Contour lines show regular forms or patterns in the two horizontal directions. The iso-slope lines appear to be slightly noisy due to the experimental technique used (see Section 3.3). The noise intensity is higher far from the light source (high values of x and y). But even if the iso-slope contours seem to be irregular, the vector map of the 2D slope field computed from the η_x and η_y values, plotted in *figure 13*, exhibits coherent patterns, where their structure can be easily seen. *Figure 14* represents the iso-elevation lines of the surface topography $\eta(x, y)$ computed with the recursive integration scheme described in Section 3.4. The patterns are aligned along the x and y directions, and troughs and crests are periodically spaced. Furthermore the crests have a rhombic form while the troughs have an elliptic form. The crests seem to be sharper than the troughs. We can also note that the crests are, in terms of absolute value, 'higher' than the troughs, i.e. $\eta_{\max} > -\eta_{\min}$. *Figure 15* is a three dimensional view of the measured topography. As mentioned previously, the crests have a sharp pyramidal-like form. This pyramidal shape is in agreement with the camera view of the wave field shown in *figure 11*. Furthermore, the measured patterns are qualitatively similar to the analytic gravity wave patterns in *figure 3(b)*.

Figure 11. Experiment n° 6: camera back view the short-crested wave field.

The directional spectral density of the wave slopes is shown in *figure 16(a)* in the $(\log(k), \theta)$ plane. The angular spreading of the energy at the dominant wavenumber is also shown (*figure 16(b)*). Clearly two peaks can be observed. The location of the maximum energy defines (a) the wavelength ($\lambda_{\text{peak}} = 7.70$ cm) and (b) the angles for the incident (left peak, $\theta_i = +34^\circ$) and the reflected (right peak, $\theta_r = -34^\circ$) wave trains. These measured values are in good agreement with the initial conditions imposed by the wavemaker for this experiment, i.e. $\lambda_i = 7.83$ cm and $\theta_i = 35^\circ$. The angular spectrum shows that no parasitic waves were present in the flow. Moreover, incident and reflected waves have nearly the same energy.

Results from the other experiments and comparisons with analytical formulations presented in Section 2 are given in the next section.

4.5. Water level comparisons

Figure 17 gives an example of the surface topography measured for each of the six run experiments listed in *table III*. Patterns present very regular forms in the two horizontal directions. Wave crests and wave troughs are aligned along oblique directions. *Figures 17(a), (b)* and *(c)* correspond to 35° incident waves, and *figures 17(d), (e)* and *(f)* to 45° incident waves. The size of the patterns clearly depends on the value of the incident

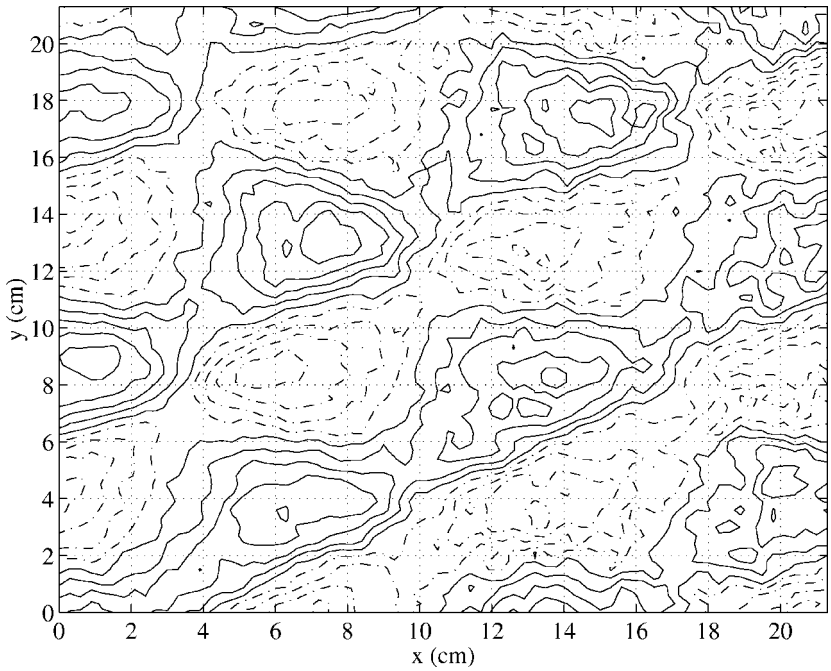

(a)

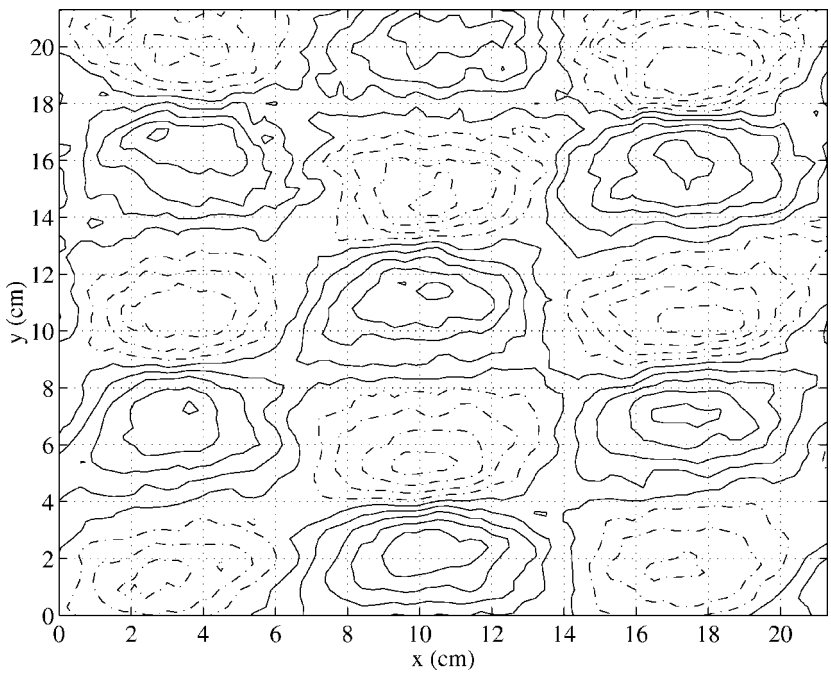

(b)

Figure 12. Experiment n° 6: iso-slope contours (a) in x-direction (range interval $[-0.42, 0.44]$), (b) in y-direction (range interval $[-0.58, 0.63]$). Solid lines for positive slopes and dashed lines for negative slopes.

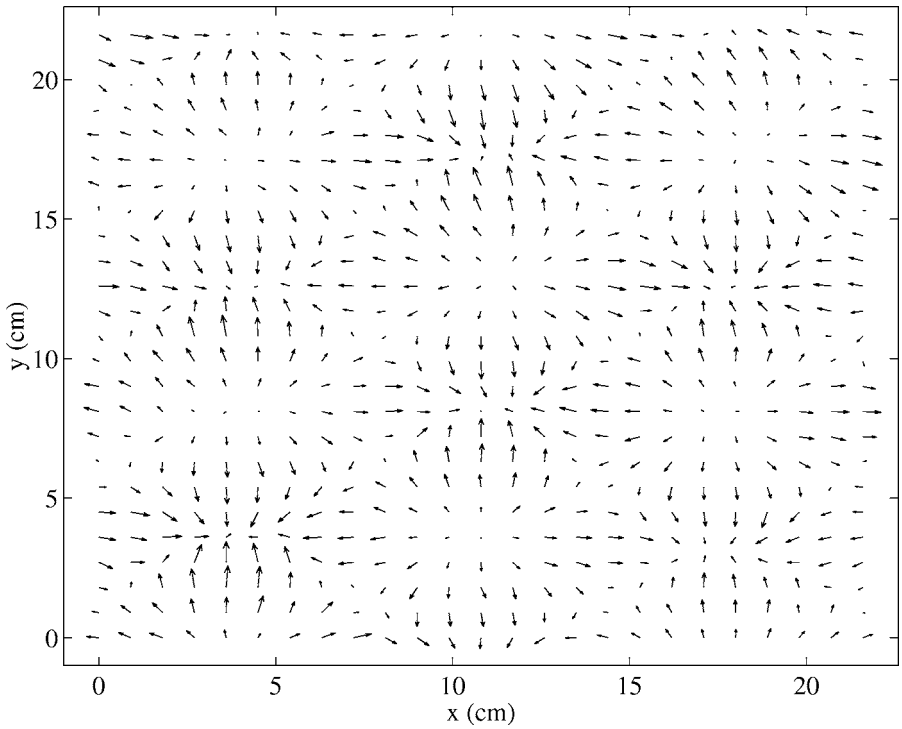

Figure 13. Experiment n° 6: vector map of the two-dimensional slope field.

wavelength (see for example *figures 17(a)* ($\lambda_i = 12.45$ cm) and *17(f)* ($\lambda_i = 7.83$ cm)). The rhombic form of the crest and the elliptic form of the troughs appear clearly on those figures.

In order to compare these experimental measurements with the theoretical developments presented in Section 2, a corresponding analytical surface was computed for each of the six experiments. The analytic input parameters, i.e. incidence angle θ_i, wavelength λ_i and incident steepness $(ak)_i$, were adjusted to the experimental incident wave conditions measured with the capacitance gauge between wharfs 1 and 3. The analytical surface topography was then computed and compared with the measured surface topography. For example, the short-crested wave field presented in *figure 18* was calculated using the input conditions of experiment n° 6. This figure, showing a theoretical surface, is very similar to the experimental n° 6 measured surface presented in *figure 15*. Only small deviations can be detected near the measured crests.

To present quantitative comparisons, we have computed the root mean square (RMS) difference between analytical and experimental surfaces over a full short-crested wave pattern for each experiment. The *RMS* values were computed over a pattern centered on a crest and over a pattern centered on a trough. The input values used for the analytical surface determination (angle θ, wavelength λ and short-crested wave steepness h) and the resulting *RMS* differences are listed in *table IV*. *RMS* errors are relatively small: all the values are less than 0.23 cm and lower than 10% of the crest-to-trough values. These results show the good accuracy of the measurements from the new optical device compared with the analytical developments.

Examples of graphic comparisons are given in *figures 19–22*. We have plotted the iso-elevation contours of the measured surface topography (solid lines), the corresponding analytical surface topography (dashed lines), and the absolute difference between the two surfaces. These figures are convenient to visualize the location where the errors are the highest. Three different classes of experiment may be noted.

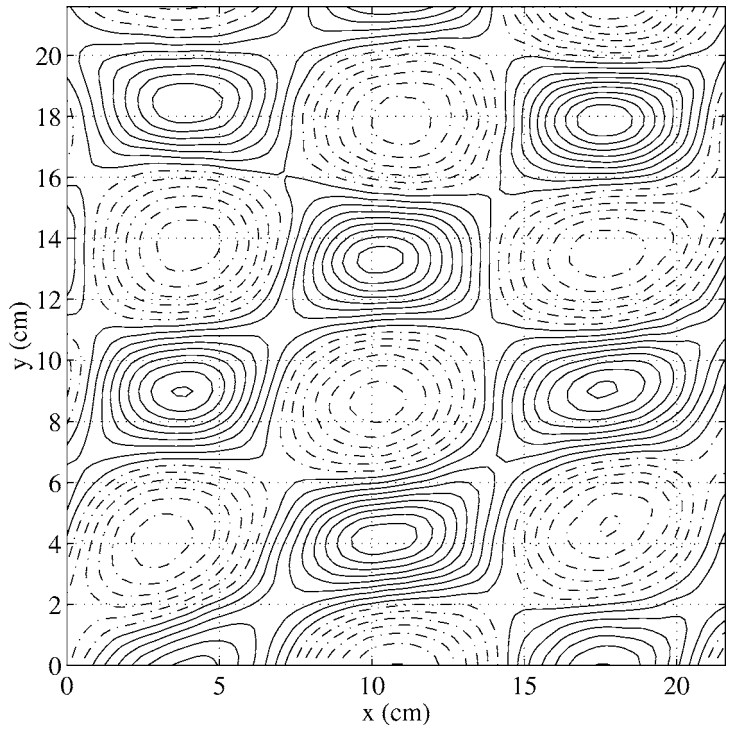

Figure 14. Experiment n° 6: surface topography; iso-elevation contours provided from the new integration method (contour interval in cm: $[-0.34, 0.44]$). Dashed lines represent the negative values and solid lines the positive values.

Table IV. RMS differences between experimental and analytical surface topographies. The input parameters (θ, λ, and h) used for the analytical computations are indicated.

Exp. n°	θ	λ (cm)	h	Area centered on	RMS difference (cm)	Crest-to-trough (cm)
1	44°50	13.24	0.603	crest	0.229	2.54
1	44°30	12.93	0.547	trough	0.207	2.25
2	45°00	10.60	0.442	crest	0.137	1.49
2	45°25	10.28	0.458	trough	0.119	1.50
3	45°00	8.90	0.378	crest	0.054	1.07
3	44°20	8.80	0.461	trough	0.070	1.29
4	35°40	12.42	0.344	crest	0.082	1.36
4	36°40	12.30	0.332	trough	0.085	1.30
5	31°25	10.00	0.336	crest	0.116	1.07
5	32°40	10.35	0.343	trough	0.111	1.13
6	32°25	7.85	0.352	crest	0.042	0.88
6	33°55	7.71	0.334	trough	0.041	0.82

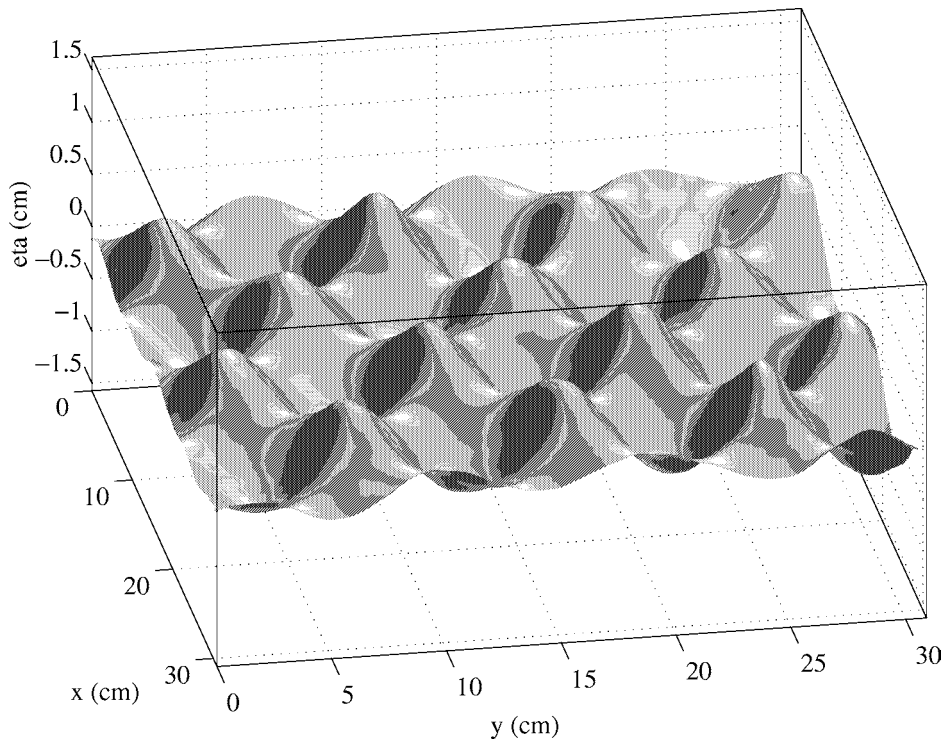

Figure 15. Experiment n° 6: three-dimensional view of the measured short-crested wave field.

The first class corresponds to the experiments with no deformation of the patterns in comparison with the analytical model (experiments n° 3, 4 and 6). Theoretical and experimental troughs and crests merge and the *RMS* errors are small, between 0.04 to 0.08 cm (cf. *figure 19* and *table IV*).

The second class includes the experiments for which the measured patterns are turned left in comparison with the model. Experiments n° 1 and 2 belong to this class. An example of comparison for run n° 1 is shown in *figure 21*. We can see clearly the differences near the four edges of the domain. *RMS* differences are much greater, they are about 0.12 to 0.23 cm. This second class corresponds to high short-crested wave steepness values h (see *table III*). This deformation might be due to three-dimensional instabilities, like those described by Su (1982) for an incident wave with steepness greater than $ak = 0.25$. There is another explanation of this discrepancy. This deformation might be due to the refraction of the incident wavetrain through the wave jump which occurs near the wall as described by Marchant and Roberts [32]. Due to the wave jump the incident wavetrain turns left and propagates slightly more parallel to the wall. Furthermore, when the waves are very steep, short-scale roughness or parasitic capillary waves appear along the waves (i.e. *figure 11*). This phenomenon could be due to three-dimensional instabilities or to curvature effects at the crest. However the image processing technique with the Wiener filter did not allow the measurement of these small scale structures.

The third class (experiment n° 5, *figure 22*), is characterized by experimental patterns having a diamond-shaped form. In this case, the location of the crests and troughs are juxtaposed with the model but the analytic and measured pyramidal forms are slightly different. *RMS* errors are about 0.11 cm.

Numerous images were digitized and analyzed for each experiment. *RMS* differences were always very small, i.e. less than 0.5 cm. Analytical and experimental potential energy per unit area were also compared. Values differed by less than 10%, which is coherent with the small quadratic errors presented in this section.

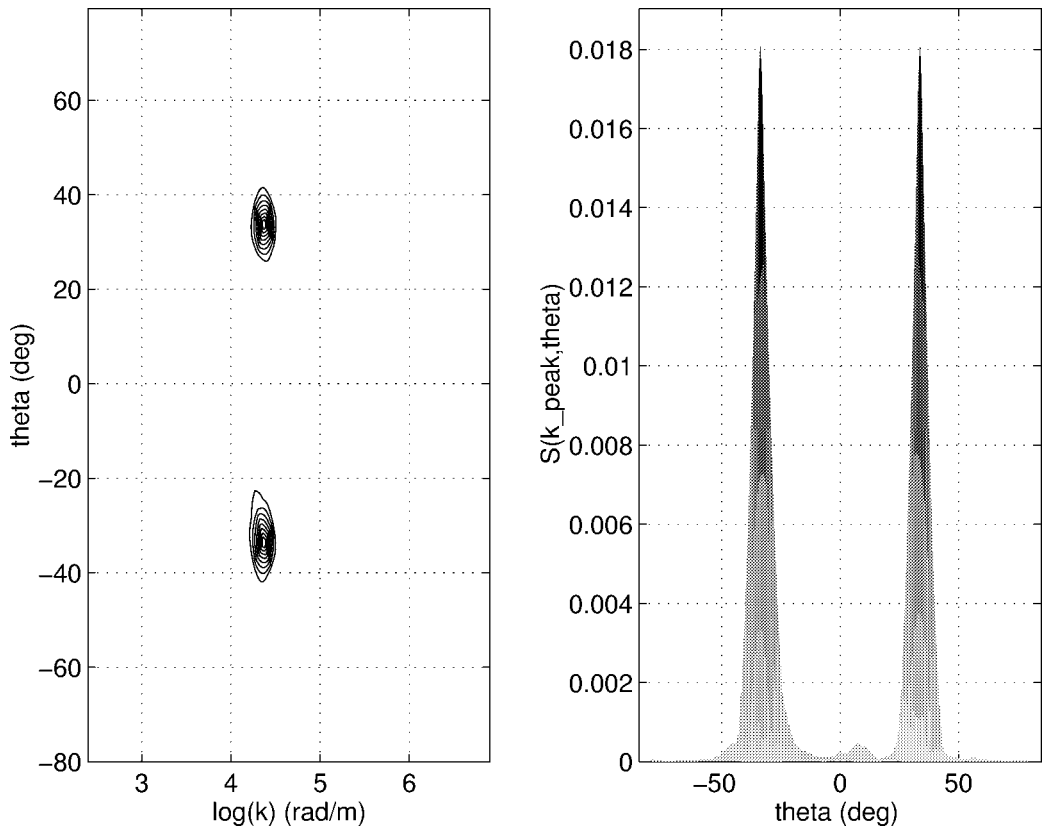

Figure 16. Experiment n° 6: (a) directional spectral density of the wave slope; (b) directional distribution at $k = k_{\text{peak}}$.

In the following paragraph, we investigate the kinematic properties of the short-crested wave train.

5. Spatio-temporal data analysis

5.1. Space-time diagrams

Images were acquired at a rate of 25 frames per second. Therefore, the measured surface elevation may be considered as a function of three variables $\eta(x, y, t)$. For a fixed ordinate value, y_{fix}, the spatio-temporal cross-section

$$\eta(x, t)_{\{y=y_{\text{fix}}\}} = \eta(x, y_{\text{fix}}, t)$$

gives information on the evolution of the wave patterns along the x axis. Similarly, for a fixed abscissa value, x_{fix}, the cross-section

$$\eta(y, t)_{\{x=x_{\text{fix}}\}} = \eta(x_{\text{fix}}, y, t)$$

refers to the evolution of the patterns along the transverse direction. An example of such cross-sections is given in *figures 23(a)* and *(b)* for experiment n° 6. *Figure 23(a)* represents the $\eta(x, t)_{\{y=y_{\text{fix}}\}}$ iso-elevation contours at $y_{\text{fix}} = 12.6$ cm. In this plot, the slope x/t is exactly the x-component of the phase velocity of the short-crested wave patterns: $c_x = x/t \simeq 65.1$ cm/s. The existence of straight lines in the (x, t) plane confirms the

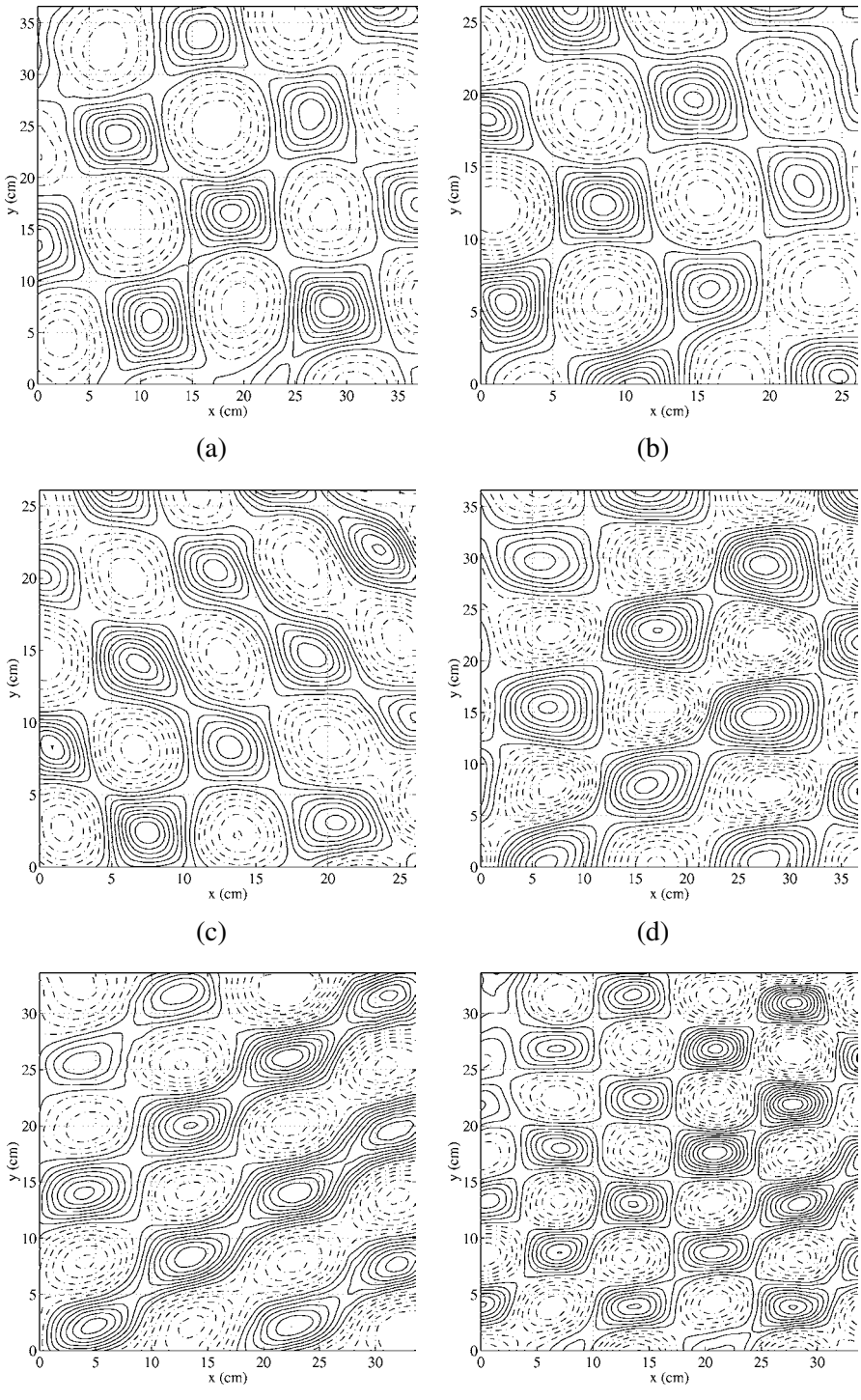

Figure 17. Typical examples of water wave iso-elevation contours for experiments listed in *table III*; (solid lines: positive elevation; dashed lines: negative elevation).

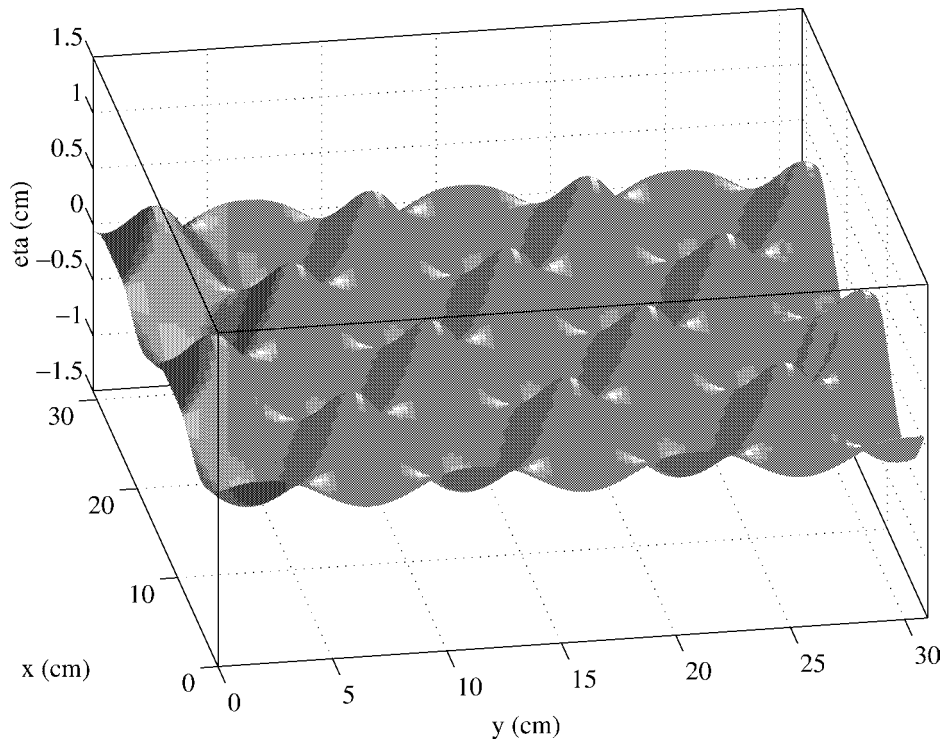

Figure 18. Three-dimensional view of the theoretical short-crested wave field for the same conditions as experiment n° 6.

steadily propagation in the x-direction of the waves. *Figure 23(b)* is the $\eta(y,t)_{\{x=x_{\text{fix}}\}}$ iso-elevation contours at $x_{\text{fix}} = 13.2$ cm. The patterns are aligned parallel to the space direction y and in the time direction t. This means that there is no transversal displacement of the patterns.

This analysis shows clearly that the short-crested wave patterns have a permanent form moving along the wharf 2 in the x-direction with no transversal oscillations.

To a more mathematical point of view, in the next paragraph we investigate the spatio-temporal properties of the short-crested wave field, using the so-called 'bi-orthogonal decomposition'.

5.2. Bi-orthogonal decomposition

To obtain statistical information on spatio-temporal data, we used a new signal processing tool. This technique is a two-dimensional generalization of the Karhumen–Loève procedure which states that a real space and time dependent signal, $u(x,t)$, may be uniquely decomposed in the form:

$$u(x,t) = \sum_k \alpha_k \phi_k(x) \psi_k(t) \tag{35}$$

with

$$\alpha_i \geqslant \alpha_j \text{ if } i < j \quad \text{and} \quad \lim_{k\to\infty} \alpha_k = 0,$$

α_k is the eigenvalue associated to the eigenvectors $\phi_k(x)$ and $\psi_k(t)$. $\{\phi_k(x)\}$ and $\{\psi_k(t)\}$ are both orthonormal eigenfunction sets called respectively 'topos' and 'chronos'. These eigenfunctions are generated by the signal

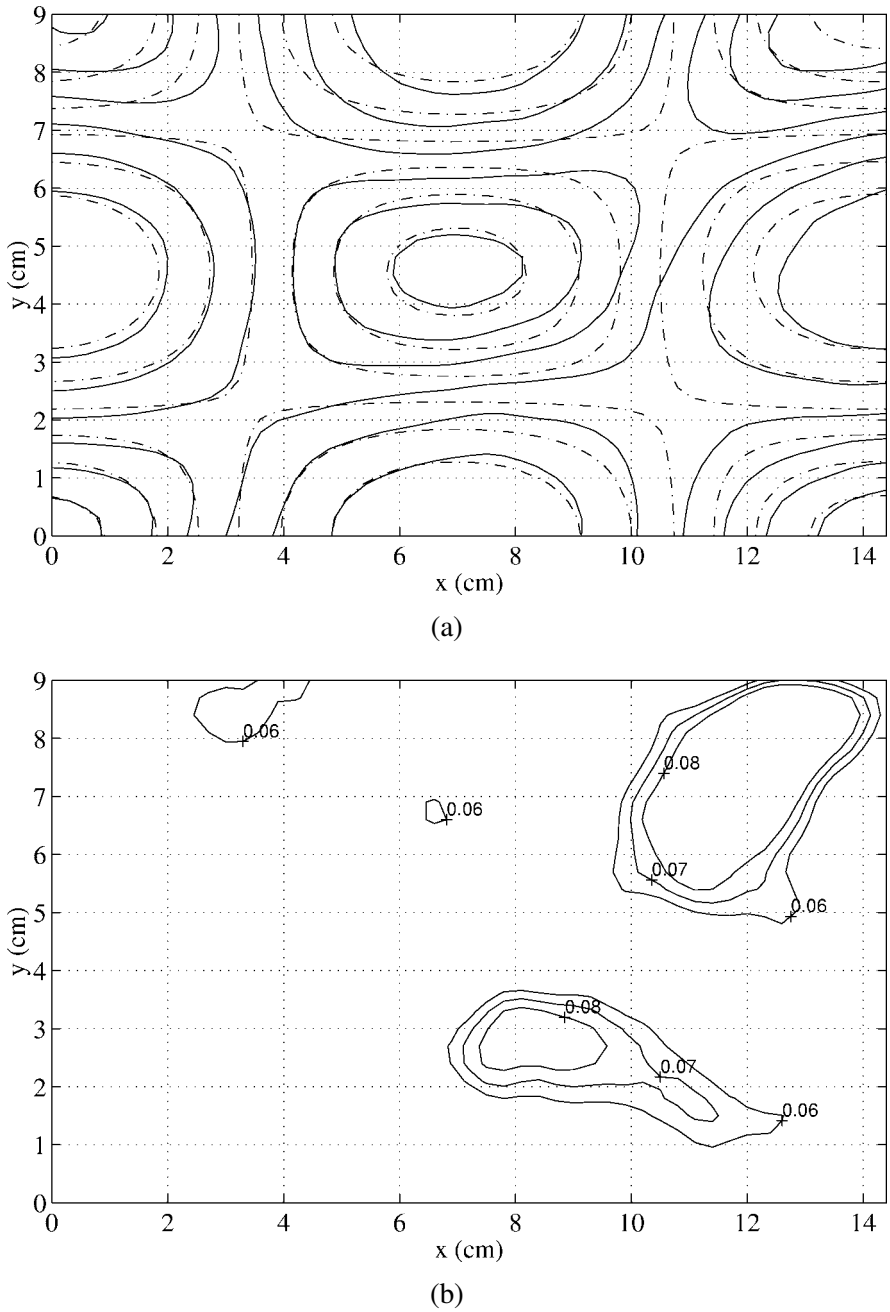

Figure 19. Experiment n° 6: (a) comparison between experimental and analytical surface topography. The area is centered on the crest of a pattern. Solid line: experimental data, dashed line: analytical data; (b) absolute difference (in cm).

itself. Topos and chronos are independent structures which compose the signal (for more details see Aubry et al. [53]).

The bi-orthogonal decomposition (35) was applied to spatio-temporal sequences constructed from successive digitized images. An example of the two first topos $\phi_1(x)$ and $\phi_2(x)$, and the two first chronos $\psi_1(t)$ and $\psi_2(t)$,

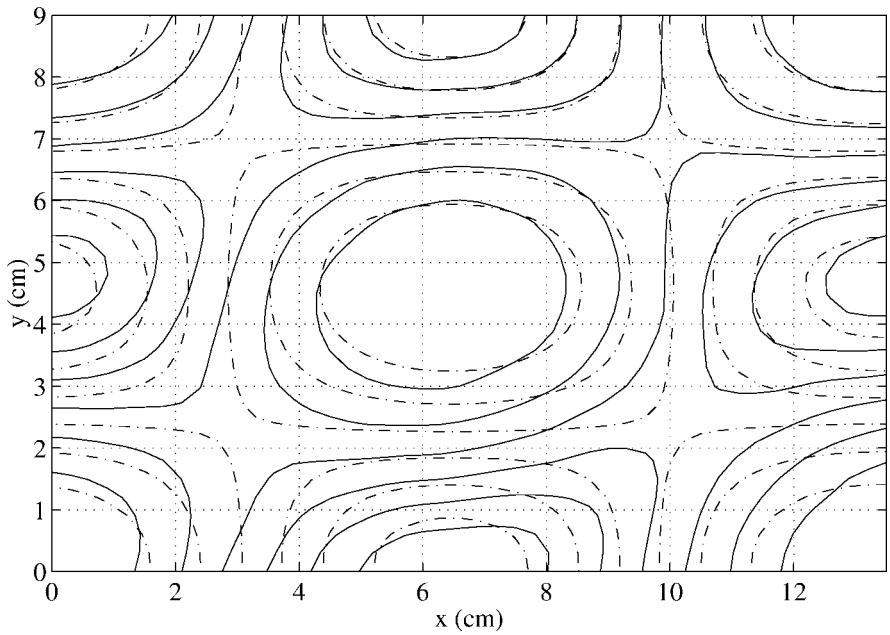

(a)

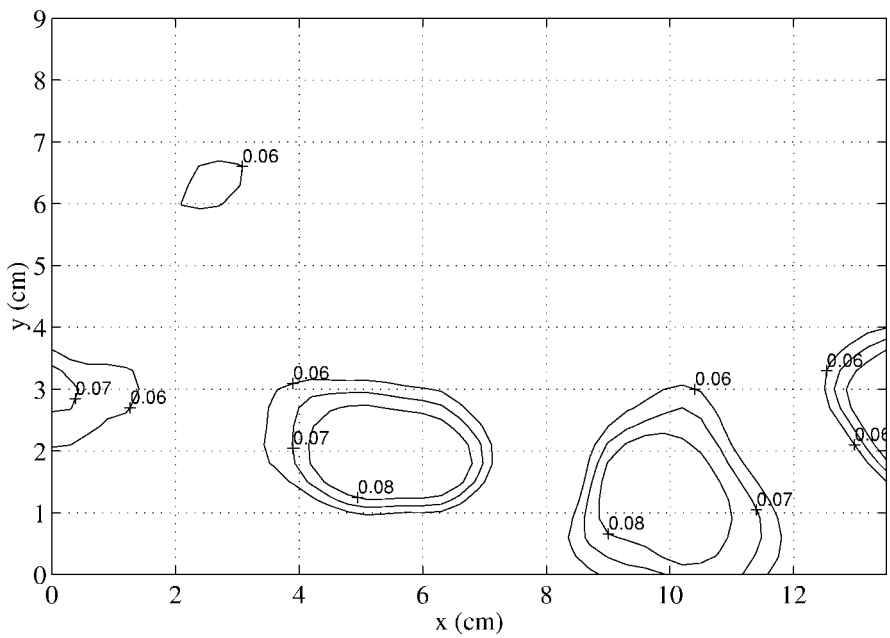

(b)

Figure 20. Experiment $n°$ 6, domain centered on a trough (see *figure19* for caption).

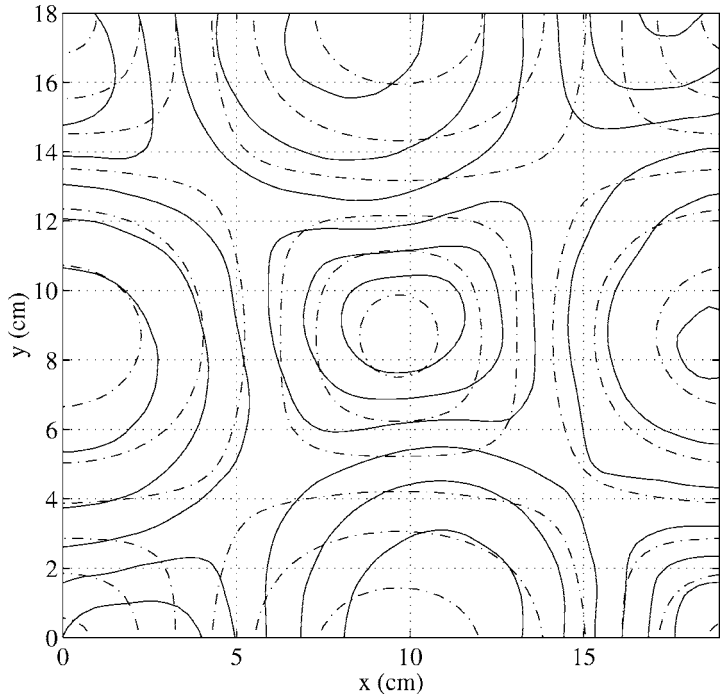

(a)

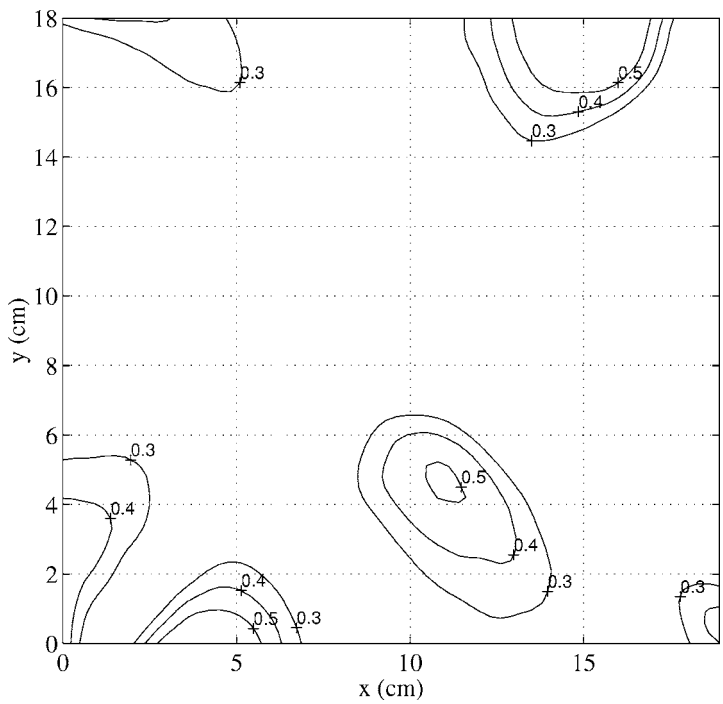

(b)

Figure 21. Experiment *n*° 1, domain centered on a crest (see *figure19* for caption).

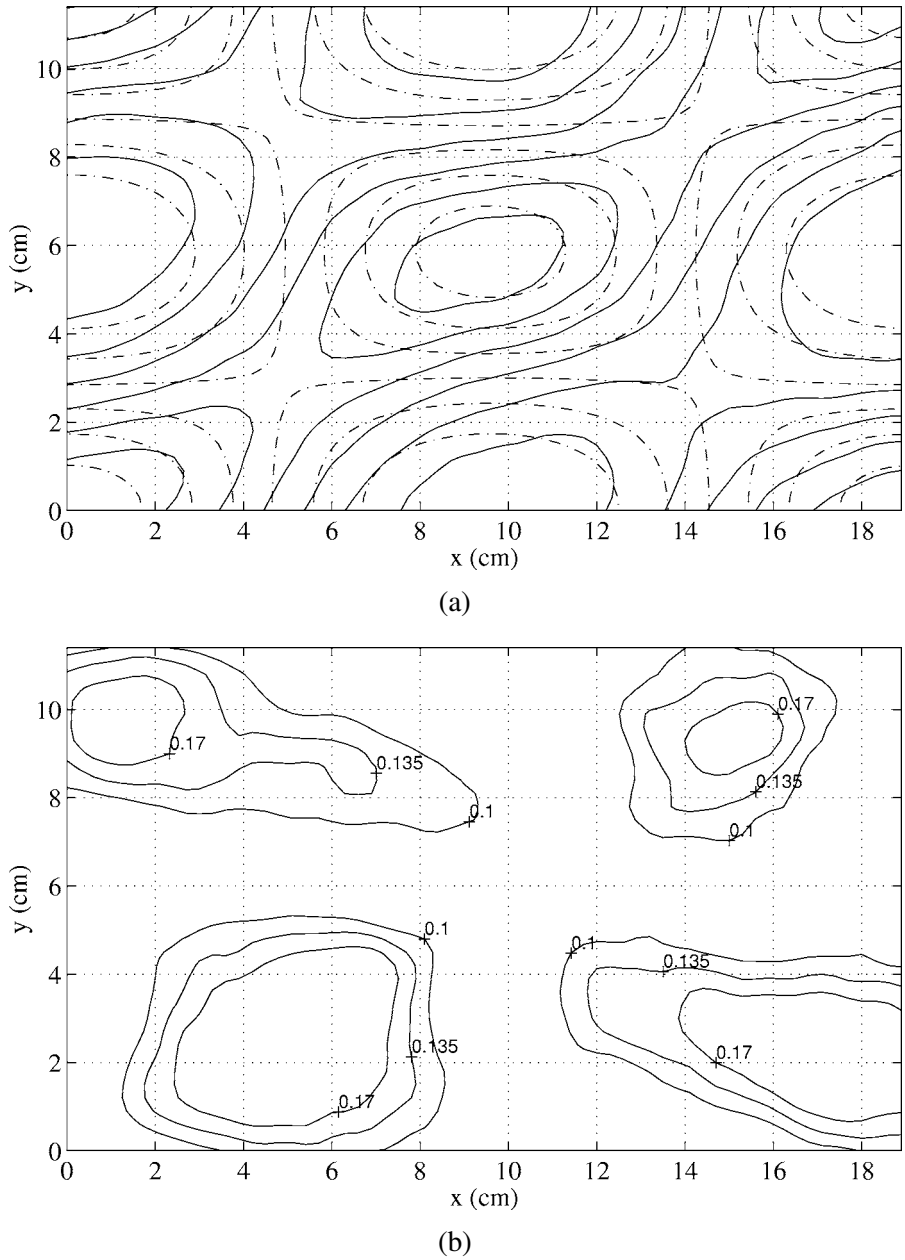

Figure 22. Experiment n° 5, domain centered on a crest (see *figure 19* for caption).

computed from the signal $\eta(x,t)_{\{y=12.6\,\mathrm{cm}\}}$, are plotted on *figure 24*. These functions seem to have a sinusoidal form with low modulations. For this experiment, the first eigenvalues $\{\alpha_k\}$ were: $\alpha_1 = 1338,\ \alpha_2 = 1247,\ \alpha_3 = 60,\ \alpha_4 = 4$. The two first eigenvalues α_1 and α_2 are much higher than α_3 and α_4. They correspond to the dominant modes.

From the bi-orthogonal decomposition, it is possible to determine the 'progressive' property of a two-dimensional wave field. Aubry et al. [53] stated the following theorem: "A signal $\eta(x,t)$ which has

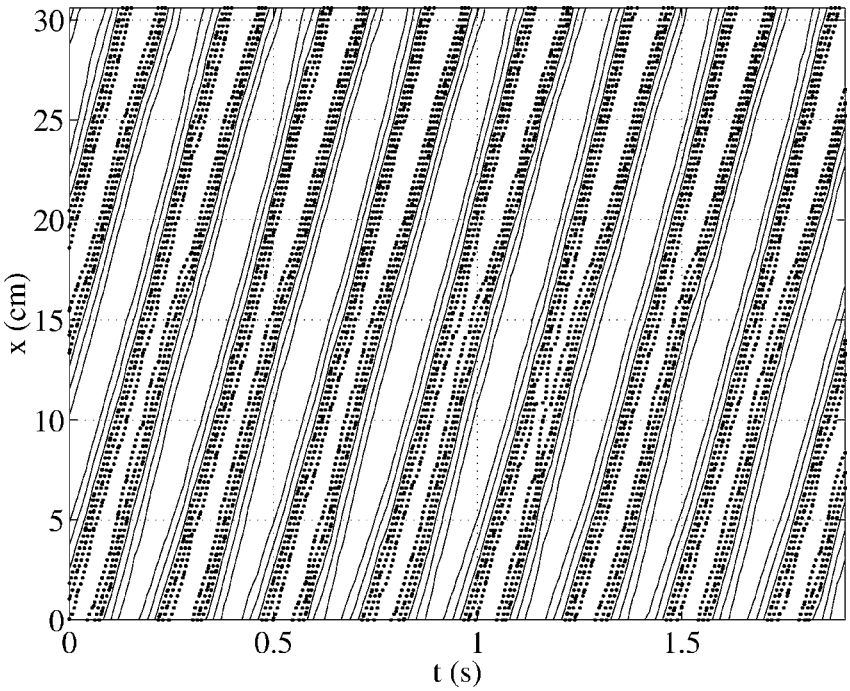

(a)

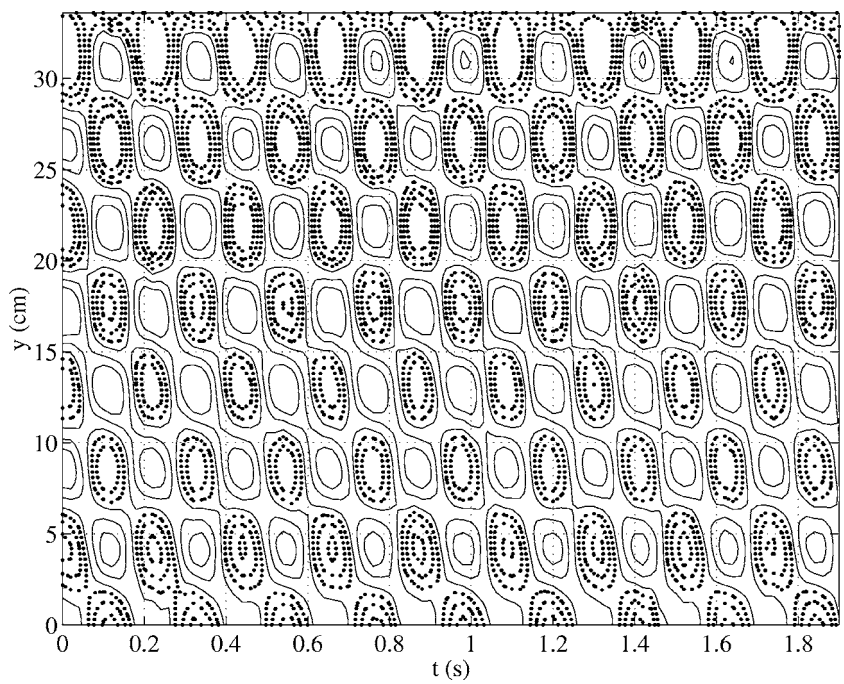

(b)

Figure 23. Experiment n° 6: spatio-temporal cross-sections of the water elevation (a) $\eta(x,t)_{\{y=12.6\,\mathrm{cm}\}}$, (b) $\eta(y,t)_{\{x=13.2\,\mathrm{cm}\}}$ (solid lines: positive values; dashed lines: negative values).

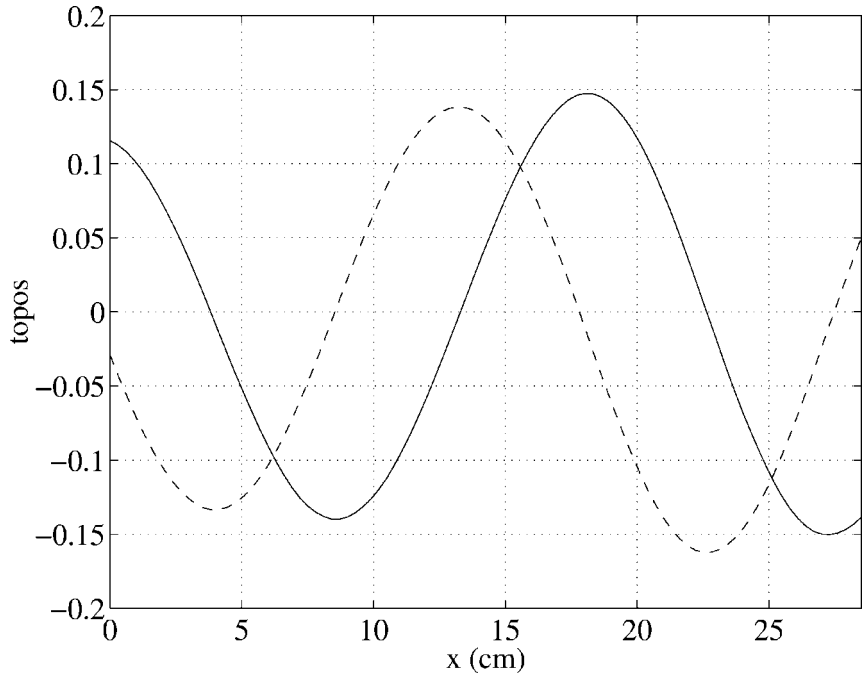

(a)

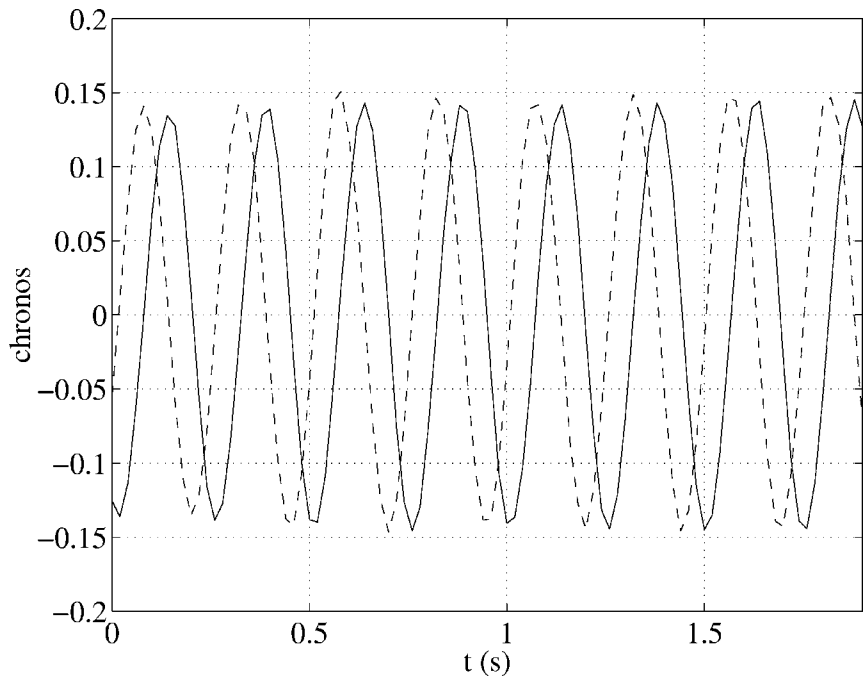

(b)

Figure 24. Experiment n° 6: bi-orthogonal decomposition of the spatio-temporal signal $\eta(x,t)_{\{y=12.6\,\mathrm{cm}\}}$ given in *figure 23*. (a) The two first topos $\phi_1(x)$ (solid line) and $\phi_2(x)$ (dashed line); (b) the two first chronos $\psi_1(t)$ (solid line) and $\psi_2(t)$ (dashed line).

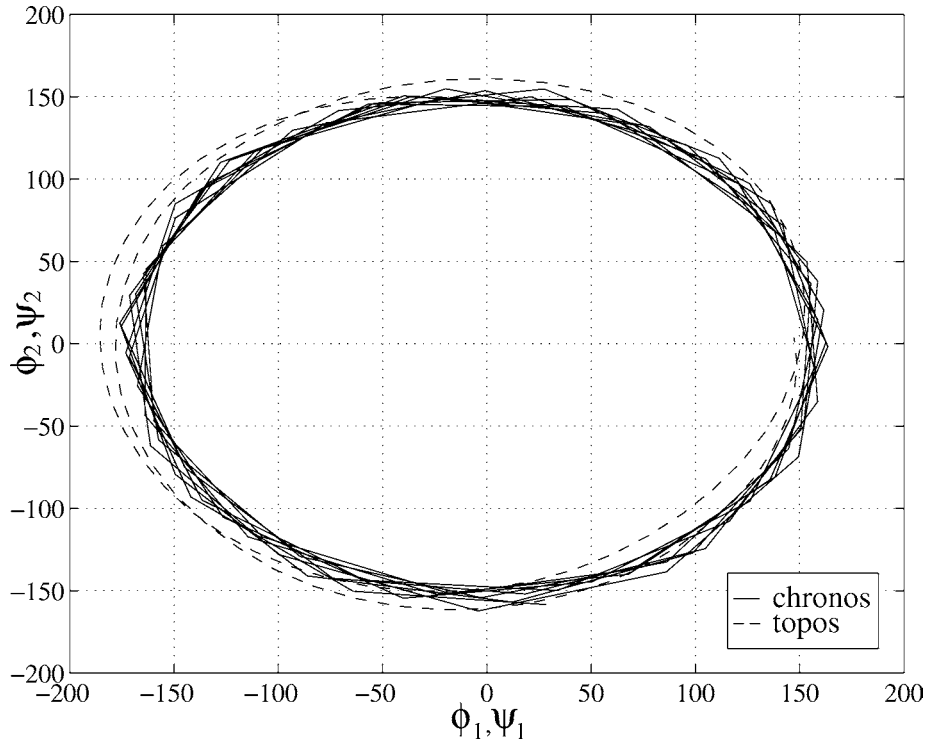

Figure 25. Experiment n° 6: plot of the topos $(\phi_1(x), \phi_2(x))$ (dashed line) and the chronos $(\psi_1(t), \psi_2(t))$ trajectories corresponding to the signal $\eta(x,t)_{\{y=12.6\text{ cm}\}}$.

two dominant modes, is a progressive wave if the trajectory $(\phi_1(x), \phi_2(x))$ merges with the trajectory $(\psi_1(t), \psi_2(t))$". To assess the progressive behavior of the short-crested waves, we have plotted in *figure 25* the $(\phi_1(x), \phi_2(x))$ and the $(\psi_1(t), \psi_2(t))$ curves on the same graph. This plot shows clearly the very good superposition of the two trajectories. Consequently, we may conclude that the short-crested wave field is progressive in the x-direction.

For the signal $\eta(y,t)_{\{x=13.2\text{ cm}\}}$, the first eigenvalues were: $\alpha_1 = 1148,\ \alpha_2 = 93,\ \alpha_3 = 45,\ \alpha_4 = 7$. Here α_1 is much higher than all the other eigenvalues. There is only one dominant mode. This means that the wave field was stationary along the y-direction, which is coherent with the remarks made in Section 5.1, i.e. no transversal oscillation along y-axis.

From the bi-orthogonal decomposition, it is also possible to determine the 'space and time periodicity' properties of a two-dimensional wave field: "a signal $\eta(x,t)$ is spatially (respectively temporally) periodic if and only if, all the topos (respectively the chronos) are periodic" (Aubry et al. [53]). We analyzed only the dominant modes, i.e. the two first modes of the signal $\eta(x,t)$ and the first mode of the signal $\eta(y,t)$. To exhibit the periodicity, we calculate the Hilbert transform of the topos and chronos. We used the Hilbert transform, because the monochromatic character of our signal was obvious.

Figure 26 shows the Hilbert transforms of $\phi_1(x)$, $\phi_2(x)$, and $\psi_1(t)$, which are the dominant modes of the spatio-temporal $\eta(x,t)$ cross-section. The imaginary part of each mode is plotted as a function of the real part. The trajectories observed on the plots are closed curves turning along the same path. These trajectories indicate clearly that the dominant topos and chronos for the $\eta(x,t)$ signal are periodic. *Figure 27* shows the Hilbert

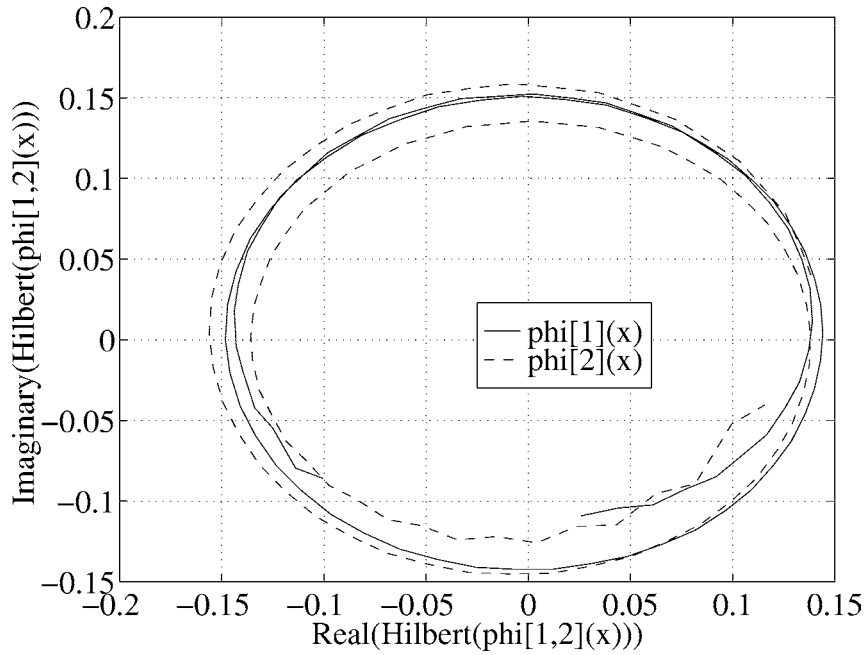

(a)

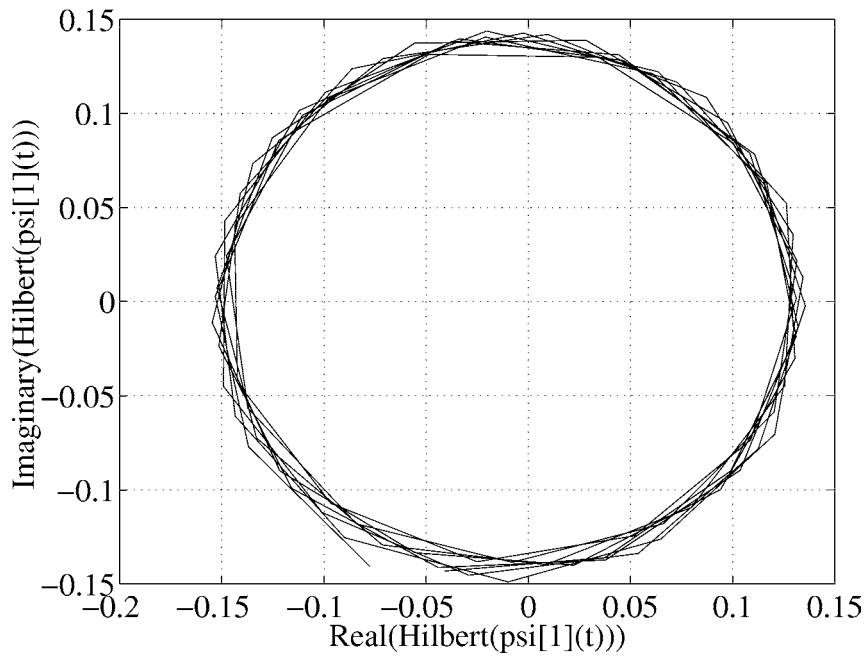

(b)

Figure 26. Experiment n° 6: Hilbert transform of the dominant modes of the bi-orthogonal decomposition of the $\eta(x,t)_{\{y=12.6\,\mathrm{cm}\}}$ cross-section. (a) Topos $\phi_1(x)$ (solid line) and $\phi_2(x)$ (dashed line); (b) chronos $\psi_1(t)$.

transforms of $\phi_1(y)$ and $\psi_1(t)$, which are the dominant modes of the $\eta(y,t)$ cross-section. Results are similar: the closed curves prove that the dominant modes are periodic.

Consequently, from the analysis of the dominant modes, we may conclude that the experiment n° 6 short-crested wave field is a periodic field of permanent form, progressive in the x-direction and stationary in the y-direction. Similar results were obtained for the other experiments, except for experiment n° 1 where no stable conditions were found. The short-crested wave steepness h for that experiment was relatively high (see *table IV*) and the waves were probably submitted to three-dimensional instabilities. Eigenvalues decrease very slowly and no obvious dominant modes were found.

The bi-orthogonal decomposition analysis is an usual tool to compute the wave celerity. The wave celerity is given by $c = \Delta x/\Delta t$, where Δx is the spatial shift between the two first topos and Δt the temporal shift between the two first chronos. The Δt and Δx values were computed using the intercorrelation functions. Comparisons between experimental and analytic results are given in *figure 28*. We observe a very good agreement. The accuracy is about 1% except for experiment n° 2 for which the difference is about 4%. The celerity of experiment n° 1 is not shown, because no stable conditions were found.

6. Conclusions

This study concerns the investigation of short-crested wave fields generated by a sea-wall reflection of an incident plane wave. First we have developed analytical solutions of the hydrodynamic equations governing the three-dimensional wave motion using a perturbation method. These analytical expressions extend previous studies on nonlinear short-crested waves up to the sixth order for capillary-gravity waves in finite depth, and up to the ninth order for gravity waves in deep water.

Experiments were then conducted in a tank. The short-crested wave field was generated by sending oblique incident paddle waves on a vertical wall. Different wavelengths, amplitudes and incidence angles were tested. We built a new video-optical tool based on the 'shape from shading' principle, with two monochromatic lights allowing the simultaneous measurement of the η_x and η_y wave slopes. We used a recursive integration procedure to estimate the surface topography $\eta(x, y, t)$.

A very good agreement was found between the analytical and experimental investigations. *RMS* differences of surface elevation differed by less than 10%. Spatio-temporal properties of the wave field were analyzed with the 'bi-orthogonal decomposition' technique. We showed that short-crested wave patterns are traveling waves of permanent form, progressive in the wall direction and stationary in the transverse direction. Because of the very good agreement between analytical and experimental investigations, a direct extension of this study would be to conduct similar experiments on short-crested waves in arbitrary depth and compare the results with the theoretical developments obtained here when the surface tension effects are taken into account (see *figure 2(b)*).

Nevertheless, some experiments corresponding to high incident wave steepness were affected by modulational instabilities. Unfortunately, the measurements were limited in space and time, and it was not possible to investigate their stability over large areas and long durations. However, from the basis of the study of Ioualalen and Kharif [54] relative to the subharmonic stability of short-crested waves in deep water, we have calculated the maximum instability growth rates for experiments conducted in the tank. These values, listed in *table V*, correspond to subharmonic instabilities of class Ib, i.e. to modulations both in the longitudinal and transversal directions. These values showed that for experiment n° 1, the subharmonic instabilities were strong enough to induce a rapid amplification of the perturbations. For that particular case, we effectively did not find a stable behavior of the patterns. The following stage would be to study a wider three-dimensional wave field using two oblique wavemakers. This is necessary to measure the evolution along different fetches and to understand the stability of high steepness short-crested wavefields.

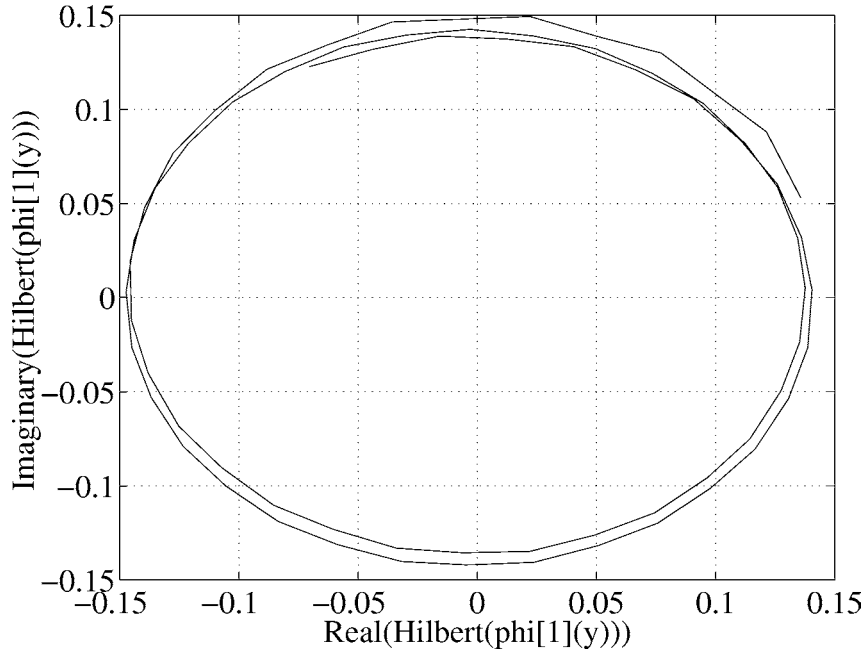

(a)

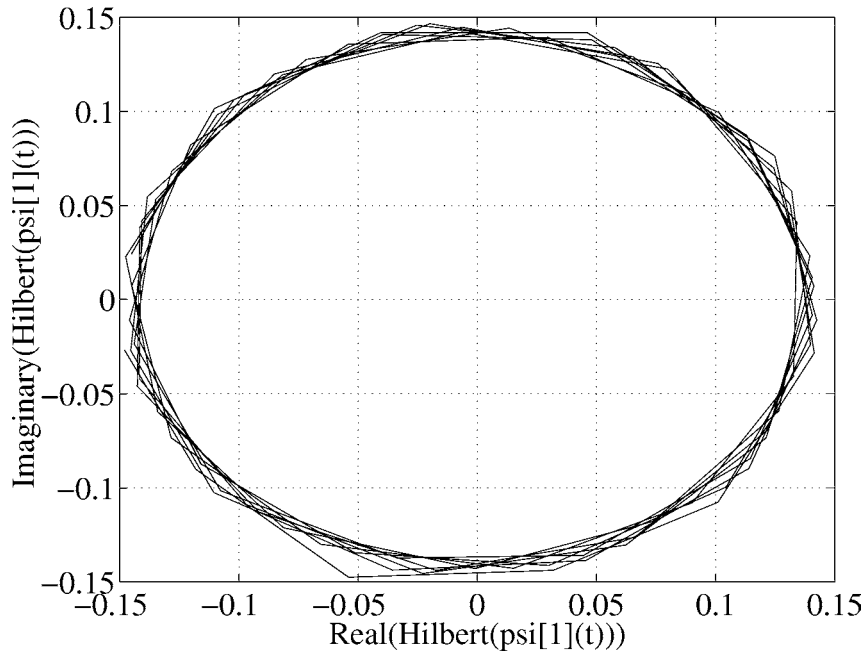

(b)

Figure 27. Experiment n° 6: Hilbert transform of the dominant modes of the bi-orthogonal decomposition of the $\eta(y,t)_{\{x=13.2\,\mathrm{cm}\}}$ section. (a) Topos $\phi_1(y)$; (b) chronos $\psi_1(t)$.

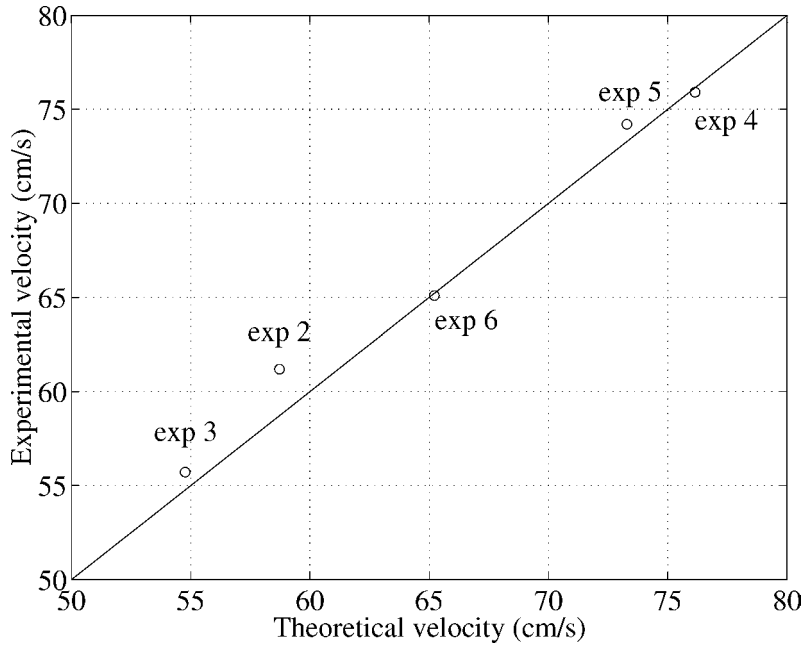

Figure 28. Comparison between theoretical and experimental celerity.

Table V. Maximum growth rates for the so-called *class Ib* instability.

Experiment	Maximum growth rate
1	0.0139
2	0.0092
3	0.0092
4	0.0040
5	0.0034
6	0.0034

Appendix A. Analytic expressions

A.1. $\phi_R^+(X, Y, 0)$ *up to the fourth order*

Expressions of $\phi_R^+(X, Y, 0)$ are presented herein up to fourth order, but were calculated up to the ninth order.

$$\phi_1^+(X, Y, 0) = 0, \tag{36}$$

$$\phi_2^+(X, Y, 0) = \left(\frac{\partial}{\partial Z}\phi_1(X, Y, 0)\right)\Big|_{Z=0} \eta_1, \tag{37}$$

$$\begin{aligned}\phi_3^+(X, Y, 0) = &\left(\frac{\partial}{\partial Z}\phi_2(X, Y, Z)\right)\Big|_{Z=0} \eta_1 + \left(\frac{\partial}{\partial Z}\phi_1(X, Y, Z)\right)\Big|_{Z=0} \eta_2 \\ &+ \frac{1}{2}\left(\frac{\partial^2}{\partial Z^2}\phi_1(X, Y, Z)\right)\Big|_{Z=0} \eta_1^2,\end{aligned} \tag{38}$$

$$\begin{aligned}\phi_4^+(X,Y,0) = &\left(\frac{\partial}{\partial Z}\phi_1(X,Y,Z)\right)\Big|_{Z=0}\eta_3 + \left(\frac{\partial}{\partial Z}\phi_2(X,Y,Z)\right)\Big|_{Z=0}\eta_2 \\ &+ \left(\frac{\partial}{\partial Z}\phi_3(X,Y,Z)\right)\Big|_{Z=0}\eta_1 + \frac{1}{6}\left(\frac{\partial^3}{\partial Z^3}\phi_1(X,Y,Z)\right)\Big|_{Z=0}\eta_1^3 \\ &+ \frac{1}{2}\left(\frac{\partial^2}{\partial Z^2}\phi_2(X,Y,Z)\right)\Big|_{Z=0}\eta_1^2 + \left(\frac{\partial^2}{\partial Z^2}\phi_1(X,Y,Z)\right)\Big|_{Z=0}\eta_1\eta_2.\end{aligned} \tag{39}$$

A.2. $\tau_R^+(X,Y)$ *up to the fourth order*

Expressions of $\tau_R^+(X,Y)$ are presented up to fourth order, but were calculated in our code up to the ninth order.

$$\tau_2^+ = 0, \tag{40}$$

$$\begin{aligned}\tau_3^+ = &-2n^2m^2\left(\frac{\partial^2}{\partial X\partial Y}\eta_1(X,Y)\right)\left(\frac{\partial}{\partial X}\eta_1(X,Y)\right)\frac{\partial}{\partial Y}\eta_1(X,Y) \\ &-\left(\frac{3m^4\frac{\partial}{\partial X}\eta_1(X,Y)^2}{2} + \frac{n^2m^2\frac{\partial}{\partial Y}\eta_1(X,Y)^2}{2}\right)\frac{\partial^2}{\partial X^2}\eta_1(X,Y) \\ &-\left(\frac{3n^4\frac{\partial}{\partial Y}\eta_1(X,Y)^2}{2} + \frac{n^2m^2\frac{\partial}{\partial X}\eta_1(X,Y)^2}{2}\right)\frac{\partial^2}{\partial Y^2}\eta_1(X,Y),\end{aligned} \tag{41}$$

$$\begin{aligned}\tau_4^+ = &-\frac{3m^4\left(\frac{\partial^2}{\partial X^2}\eta_2(X,Y)\right)\frac{\partial}{\partial X}\eta_1(X,Y)^2}{2} - \frac{n^2m^2\left(\frac{\partial^2}{\partial X^2}\eta_2(X,Y)\right)\frac{\partial}{\partial Y}\eta_1(X,Y)^2}{2} \\ &-\frac{n^2m^2\left(\frac{\partial^2}{\partial Y^2}\eta_2(X,Y)\right)\frac{\partial}{\partial X}\eta_1(X,Y)^2}{2} - \frac{3n^4\left(\frac{\partial^2}{\partial Y^2}\eta_2(X,Y)\right)\frac{\partial}{\partial Y}\eta_1(X,Y)^2}{2} \\ &-2n^2m^2\left(\frac{\partial^2}{\partial X\partial Y}\eta_1(X,Y)\right)\left(\frac{\partial}{\partial X}\eta_1(X,Y)\right)\frac{\partial}{\partial Y}\eta_2(X,Y) \\ &-2n^2m^2\left(\frac{\partial^2}{\partial X\partial Y}\eta_1(X,Y)\right)\left(\frac{\partial}{\partial X}\eta_2(X,Y)\right)\frac{\partial}{\partial Y}\eta_1(X,Y) \\ &-2n^2m^2\left(\frac{\partial^2}{\partial X\partial Y}\eta_2(X,Y)\right)\left(\frac{\partial}{\partial X}\eta_1(X,Y)\right)\frac{\partial}{\partial Y}\eta_1(X,Y) \\ &+\left(-3n^4\left(\frac{\partial}{\partial Y}\eta_1(X,Y)\right)\frac{\partial}{\partial Y}\eta_2(X,Y) - n^2m^2\left(\frac{\partial}{\partial X}\eta_1(X,Y)\right)\frac{\partial}{\partial X}\eta_2(X,Y)\right)\frac{\partial^2}{\partial Y^2}\eta_1(X,Y) \\ &+\left(-3m^4\left(\frac{\partial}{\partial X}\eta_1(X,Y)\right)\frac{\partial}{\partial X}\eta_2(X,Y) - n^2m^2\left(\frac{\partial}{\partial Y}\eta_1(X,Y)\right)\frac{\partial}{\partial Y}\eta_2(X,Y)\right)\frac{\partial^2}{\partial X^2}\eta_1(X,Y).\end{aligned} \tag{42}$$

Apendix B. Expressions of $\eta_2(X,Y)$, $\phi_2(X,Y,Z)$ and ω_2

$$\begin{cases}\eta_2 = a_{2,20}\cos(2X) + a_{2,22}\cos(2X)\cos(2Y) + a_{2,02}\cos(2Y) + a_{2,00}, \\ \phi_2 = a_{2,20}\sin(2X)\cosh\big(\alpha_{20}(Z+d)\big) + a_{2,22}\sin(2X)\cos(2Y)\cosh\big(\alpha_{22}(Z+d)\big),\end{cases} \tag{43}$$

$$a_{2,20} = \frac{(-3\omega_M^2\omega_0^4 + (2m\omega_M^4 + 2m(1+\kappa)^2)\omega_0^2 + (-1+2m^2)(1+\kappa)^2\omega_M^2)m(1+\kappa)}{(8(\omega_M^4 + (1+\kappa)^2)\omega_0^2 - 8m\omega_M^2(1+\kappa)(1+4\kappa m^2))\omega_0^2}, \tag{44}$$

$$a_{2,22} = -\frac{(-\omega_0^4 + 3(1+\kappa)^2)(1+\kappa)}{8\,\omega_0^2(3\,\kappa\,(1+\kappa) - \omega_0^4)}, \tag{45}$$

$$a_{2,00} = \frac{\omega_0^2}{8} - \frac{(1+\kappa)^2}{8\,\omega_0^2}, \tag{46}$$

$$a_{2,02} = -\frac{\omega_0^2}{-8 - 32\,\kappa + 32\,\kappa\,m^2} + \frac{(-1+2\,m^2)(1+\kappa)^2}{(-8 - 32\,\kappa + 32\,\kappa\,m^2)\omega_0^2}, \tag{47}$$

$$b_{2,20} = \frac{(-\omega_M^4 + (1+\kappa)^2)(-3\,\omega_0^4 + (-1+2\,m)(1+2\,m)(1+\kappa)(2\,\kappa\,m^2 + \kappa + 1))}{16\,\omega_0((\omega_M^4 + (1+\kappa)^2)\omega_0^2 - m\omega_M^2(1+\kappa)(1+4\,\kappa\,m^2))}, \tag{48}$$

$$b_{2,22} = -\frac{(3\,(1+\kappa)^2 - 3\,\omega_0^4)(-\omega_0^4 + (1+\kappa)(3\,\kappa+1))}{16\,\omega_0^3(3\,\kappa\,(1+\kappa) - \omega_0^4)}, \tag{49}$$

$$\omega_2 = n\omega_2/d\omega_2, \tag{50}$$

$$\begin{aligned}
n\omega_2 = {} & \big((16\,\kappa\,\omega_M^4 + 16\,\kappa\,(1+\kappa)^2)m^2 + (-16\,\kappa - 6)\omega_M^4 - 2\,(8\,\kappa+3)(1+\kappa)^2\big)\omega_0^{14} \\
& + (-64\,(1+\kappa)\kappa^2\omega_M^2 m^5 + 64\,\kappa\,(\kappa-1)(1+\kappa)\omega_M^2 m^3 + 8\,(1+\kappa)(11\,\kappa+3)\omega_M^2 m)\omega_0^{12} \\
& + \big((64\,\kappa^2\omega_M^4 + 64\,\kappa^2(1+\kappa)^2)m^6 + (-16\,\kappa\,(3+10\,\kappa)\omega_M^4 - 16\,\kappa\,(3+10\,\kappa)(1+\kappa)^2)m^4 \\
& + ((16 + 24\,\kappa^2 + 36\,\kappa - 80\,\kappa^3)\omega_M^4 - 4\,(-4 - 6\,\kappa^2 - 9\,\kappa + 20\,\kappa^3)(1+\kappa)^2)m^2 + (80\,\kappa^3 \\
& + 5 + 54\,\kappa + 102\,\kappa^2)\omega_M^4 + (80\,\kappa^3 + 5 + 54\,\kappa + 102\,\kappa^2)(1+\kappa)^2\big)\omega_0^{10} + \big(-256\,\kappa^3(1+\kappa) \\
& \times \omega_M^2 m^9 + 512\,\kappa^2(1+\kappa)(2\,\kappa+1)\omega_M^2 m^7 + 16\,\kappa\,(1+\kappa)(20\,\kappa^3 - 24\,\kappa^2 - 11\,\kappa + 5)\omega_M^2 m^5 \\
& - 16\,(1+\kappa)(20\,\kappa^4 + 16\,\kappa^3 + 27\,\kappa^2 + 23\,\kappa + 4)\omega_M^2 m^3 - (1+\kappa)(248\,\kappa^3 + 264\,\kappa^2 + 36\,\kappa \\
& - 7)\omega_M^2 m\big)\omega_0^8 + \big((-128\,\kappa^2(1+\kappa)^2\omega_M^4 - 128\,\kappa^2(1+\kappa)^4)m^8 + (-64\,\kappa\,(1+\kappa)(2\,\kappa^2+1) \\
& \times \omega_M^4 - 64\,\kappa\,(2\,\kappa^2+1)(1+\kappa)^3)m^6 + (8\,(1+\kappa)(71\,\kappa^3 + 45\,\kappa^2 + 18\,\kappa + 2)\omega_M^4 + 8\,(71\,\kappa^3 \\
& + 45\,\kappa^2 + 18\,\kappa + 2)(1+\kappa)^3)m^4 + (4\,\kappa\,(1+\kappa)(28\,\kappa^3 - 41\,\kappa^2 - 10\,\kappa - 4)\omega_M^4 + 4\,\kappa\,(28\,\kappa^3 \\
& - 41\,\kappa^2 - 10\,\kappa - 4)(1+\kappa)^3)m^2 - (1+\kappa)(112\,\kappa^4 + 190\,\kappa^3 + 249\,\kappa^2 + 106\,\kappa + 16)\omega_M^4 \\
& - (112\,\kappa^4 + 190\,\kappa^3 + 249\,\kappa^2 + 106\,\kappa + 16)(1+\kappa)^3\big)\omega_0^6 + \big(768\,\kappa^4(1+\kappa)^2\omega_M^2 m^9 - 1536\,\kappa^3 \\
& \times (2\,\kappa+1)(1+\kappa)^2\omega_M^2 m^7 - 16\,(28\,\kappa^5 - 91\,\kappa^4 - 11\,\kappa^3 + 20\,\kappa^2 - 5\,\kappa - 1)(1+\kappa)^2\omega_M^2 m^5 \\
& + 16\,(28\,\kappa^5 + 65\,\kappa^4 + 139\,\kappa^3 + 74\,\kappa^2 + 7\,\kappa - 1)(1+\kappa)^2\omega_M^2 m^3 - 3\,(8\,\kappa^4 + 36\,\kappa^3 \\
& - 21\,\kappa^2 - 28\,\kappa - 6)(1+\kappa)^2\omega_M^2 m)\omega_0^4 + \big((384\,\kappa^3(1+\kappa)^3\omega_M^4 + 384\,\kappa^3(1+\kappa)^5)m^8 \\
& + (-192\,\kappa^2(\kappa-1)(1+\kappa)^3\omega_M^4 - 192\,\kappa^2(\kappa-1)(1+\kappa)^5)m^6 + (-24\,\kappa\,(11\,\kappa^2 + 16\,\kappa + 2) \\
& \times (1+\kappa)^3\omega_M^4 - 24\,\kappa\,(11\,\kappa^2 + 16\,\kappa + 2)(1+\kappa)^5)m^4 + (-12\,\kappa\,(4\,\kappa^2 + 5\,\kappa + 3)(1+\kappa)^4 \\
& \times \omega_M^4 - 12\,\kappa(4\,\kappa^2 + 5\,\kappa + 3)(1+\kappa)^6)m^2 + 3\,(16\,\kappa^3 + 50\,\kappa^2 + 25\,\kappa + 3)(1+\kappa)^4\omega_M^4 \\
& + 3\,(16\,\kappa^3 + 50\,\kappa^2 + 25\,\kappa + 3)(1+\kappa)^6\big)\omega_0^2 + 48\,\kappa\,(4\,\kappa^3 + 9\,\kappa^2 - 1)(1+\kappa)^5\omega_M^2 m^5 \\
& - 48\,\kappa\,(4\,\kappa^3 + 9\,\kappa^2 - 1)(1+\kappa)^5\omega_M^2 m^3 - 9\,(8\,\kappa^3 + 20\,\kappa^2 + 9\,\kappa + 1)(1+\kappa)^5\omega_M^2 m,
\end{aligned} \tag{51}$$

$$d\omega_2 = 64\,\omega_0^3(-1-4\kappa+4\kappa\,m^2)(3\kappa+3\kappa^2-\omega_0^4),$$
$$(\omega_0^2((1+\kappa)^2+\omega_M^4)-m\omega_M^2(1+\kappa)(1+4m^2\kappa))(1+\kappa) \tag{52}$$

with $\omega_M^2 = (1+\kappa)\tanh(md)$

Acknowledgements

The work was supported by ONR under contracts N00014-93-1-0500, N00014-93-1-0532. We are grateful to B. Zucchini, A. Laurence and R. Vaudo for their laboratory assistance.

References

[1] Fuchs R.A., On the theory of short-crested oscillatory waves. Gravity waves, Nat. Bur. Stand. Circular 521 (1952) 187–200.
[2] Chappelear J.E., On the description of short-crested waves, U.S. Beach Erosium Board Tech. Memo. 125, 1961.
[3] Hsu J.R., Tsuchiya Y., Silvester R., Third-order approximation to short-crested waves, J. Fluid Mech. 90 (1979) 179–196.
[4] Roberts A.J., Highly nonlinear short-crested waves, J. Fluid Mech. 135 (1983) 301–321.
[5] Marchant T.R., Roberts A.J., Properties of short-crested waves in water of finite depth, J. Austr. Math. Soc. Ser. 29 (1987) 103–125.
[6] Fenton J.D., Short-crested waves and the wave forces on a wall, J. Waterw. Port. C-ASCE. 111 (1985) 693–718.
[7] Ioualalen M., Approximation au quatrième ordre d'onde de gravité 3-D en profondeur infinie, C.R. Acad. Sci. 316 (2) (1993) 1192–1200.
[8] Reeder J., Shinbrot M., Three-dimensional, nonlinear wave interaction in water of constant depth, Nonlinear Anal-Theor. 5 (3) (1981) 303–323.
[9] Roberts A.J., Schwartz L.W., The calculation of nonlinear short-crested waves, Phys. Fluid. 26 (9) (1983) 2388–2392.
[10] Zakharov V.E., Stability of periodic waves of finite amplitude on the surface of a deep fluid, Zhurnal Prikladnoi Mekhaniki i Tekhnicheskoi Fisiki 9 (2) (1968) 86–94.
[11] Badulin S.I., Shrira V.I., Kharif C., Ioualalen M., On two approaches to the problem of instability of short-crested waves, J. Fluid Mech. 303 (1995) 297–326.
[12] Ioualalen M., Etude de la stabilité linéaire d'ondes de gravité progressives 3-D en profondeur infinie, PhD thesis, Université d'Aix-Marseille, 1989.
[13] Benjamin T.B., Impulse, flow force and variational principles, J. Appl. Math. 32 (1984) 3–68.
[14] Zufiria J.A., Symmetry breaking in periodic and solitary gravity-capillary waves on water of finite depth, J. Fluid Mech. 184 (1987) 183–206.
[15] Bridges T., Dias F., Menasce D., Steady three-dimensional finite-depth on the ocean surface: a new characterization of short-crested Stokes waves interacting with a mean flow, Preprint, 1998.
[16] Bridges T.J., Periodic patterns, linear instability, symplectic structure and mean-flow dynamics for threedimensional surface waves, Philos. T. Roy. Soc. A (1995) 1–46.
[17] Saffman P.G., Yuen H.C., A new type of three-dimensional deep-water wave of permanent form, J. Fluid Mech. 101 (1980) 797–808.
[18] Ma Y.C., On steady three-dimensional deep water weakly nonlinear gravity waves, Wave Motion 4 (1982) 113–125.
[19] Meiron D.I., Saffman P.G., Yuen H.C., The instability and breaking of deep-water waves, J. Fluid Mech. 115 (1982) 165–185.
[20] Martin D.U., Two-dimensional bifurcation of Stokes waves, Wave Motion 4 (1982) 209–219.
[21] Bryant P.J., Doubly periodic progressive permanent waves in deep water, J. Fluid Mech. 161 (1985) 27–42.
[22] Su M.Y., Three-dimensional deep-water waves. Part 1. Experimental measurement of skew and symmetric waves patterns, J. Fluid Mech. 124 (1982) 73–108.
[23] Su M.Y., Bergin M., Marler P., Myrick R., Experiments of nonlinear instabilities and evolution of steep gravity wave trains, J. Fluid Mech. 124 (1982) 45–72.
[24] Perroud P.H., The solitary wave reflection along a straight vertical wall at oblique incidence, Univ. of California, Berkeley, IER Tech. Rep. 99-3, 1957.
[25] Chen T.C., Experimental study on the solitary wave reflection along a straight sloped wall at oblique angle of incidence, U.S. Beach Erosion Board Tech. Memo. 124, 1961.
[26] Nielsen A.H., Diffraction of periodic waves along a vertical breakwater for small angles of incidence, Univ. of California, Berkeley, IER Tech. Rep., HEL-1-2, 1962.
[27] Berger U., Kohlhase S., Mach reflection as a diffraction problem, 15th Conf. Coastal Eng., 1976.
[28] Hammack J., Sheffner N., Segur H., Two-dimensional periodic waves in shallow water, J. Fluid Mech. 209 (1989) 567–589.
[29] Hammack J., McCallister D., Sheffner N., Segur H., Two-dimensional periodic waves in shallow water. Part 2. Asymmetric waves, J. Fluid Mech. 285 (1995) 95–122.
[30] Wiegel R.L., Water wave equivalent of Mach reflection, in: 9th Conf. Coastal Eng., 1964, pp. 82–102.
[31] Whitham G.B., Linear and Nonlinar Waves, Wiley-Interscience, 1974.

[32] Marchant T.R., Roberts A.J., Reflection of nonlinear deep-water waves incident onto a wedge of arbitrary angle, J. Austr. Math. Soc. Ser. 32 (1990) 61–96.
[33] Marchant T.R., Roberts A.J., A variational approach to the problem of deep-water waves forming a circular caustic, J. Fluid Mech. 194 (1988) 581–597.
[34] Peregrine D.H., Refraction of finite-amplitude water waves: deep-water waves approaching circular caustic, J. Fluid Mech. 109 (1981) 63–74.
[35] Kimmoun O., Etude théorique et expérimentale des champs de vagues à courtes crêtes, PhD thesis, Université de la Méditerranée, IRPHE, 1997.
[36] Shemdin O.H., Tran H.M., Wu S.C., Directional measurement of short ocean waves with stereophotography, J. Geophys. Res. 93 (1988) 13891–13901.
[37] Bock E.J., Hara T., Optical measurements of capillary-gravity waves spectra using a Scanning Laser Slope Gauge, J. Atmos. Ocean. Tech. 12 (1995) 395–403.
[38] Jähne B., Riemer K.S., Two-dimensional wave number spectra of small-scale water surface waves, J. Geophys. Res. 95 (1990) 11531–11546.
[39] Banner M.L., Jones I.S.F., Trinder J.C., Wavenumber spectra of short gravity waves, J. Fluid Mech. 198 (1989) 321–344.
[40] Jähne B., Schultz H., Calibration and accuracy of optical slope measurements for short wind waves, in: SPIE proceedings, Optics of the air-sea interface: theory and measurements 1749, 1992.
[41] Branger H., Maille P., Bonmarin P., Métrologie des ondes de surface, First International Symposium on Scientific Imagery and Image Proceedings, Nice, April 1995, pp. 150–154.
[42] Keller W.C., Gotwols B.L., Two-dimensional optical measurement, Appl. Optics 22 (1983) 3476–3478.
[43] Jähne B., Waas S., Optical measuring technique for small scale water surface waves, International Congress on Optical Sciences, SPIE Proceedings 1129, 1989.
[44] Keller M.R., Gotwols B.L., Plant W.J., Keller W.C., Comparison of optically-derived spectral densities and microwave cross sections in a wind-wave tank, J. Geophys. Res. 100-C8 (1995) 16163–16178.
[45] Zhang X., Cox C.S., Measuring the two-dimensional structure of a wavy water surface optically: A surface gradient detector, Exp. Fluids 17 (1994) 225–237.
[46] Zhang X., Capillary-gravity and capillary waves generated in a wind-wave tank: observations and theories, J. Fluid Mech. 289 (1995) 51–82.
[47] Coantic M., Ramamonjiarisoa A., Mestayer P., Resh F., Favre A., Wind-wave simulation of small-scale ocean-atmosphere interactions, J. Geophys. Res. 86 (1981) 391–405.
[48] Mc Lean W.K., Ma Y.C., Martin D.V., Saffman P.G., Yuen H.C., Three-dimensional instability of finite-amplitude water waves, Phys. Rev. Lett. 46 (1981) 817–820.
[49] Mc Lean W.K., Instabilities of finite-amplitude water waves, J. Fluid Mech. 114 (1982) 315–330.
[50] Benjamin T.B., Feir J.E., The disintegration of wave trains on deep water, J. Fluid Mech. 27 (1967) 417–430.
[51] Lake B.M., Yuen H.C., Nonlinear deep-water waves: theory and experiment, J. Fluid Mech. 83 (1977) 49–74.
[52] Melville W.K., Calculation of three-dimensional deep-water waves, J. Fluid Mech. 124 (1982) 109–121.
[53] Aubry N., Guyonnet R., Lima R., Spatio-temporal analysis of complex signals: theory and applications, J. Stat. Phys. 64 (1991) 1–37.
[54] Ioualalen M., Kharif C., On the subharmonic instabilities of steady three-dimensional deep water waves, J. Fluid Mech. 262 (1994) 265–291.